CELLULAR NEUROSCIENCE

CGG repeat RNA G-quadruplexes interact with FMRpolyG to cause neuronal dysfunction in fragile X-related tremor/ataxia syndrome

Sefan Asamitsu[1]*, Yasushi Yabuki[1,2]*, Susumu Ikenoshita[1,3], Kosuke Kawakubo[1,2], Moe Kawasaki[1,2], Shingo Usuki[4], Yuji Nakayama[5], Kaori Adachi[6], Hiroyuki Kugoh[7,8], Kazuhiro Ishii[9], Tohru Matsuura[10], Eiji Nanba[11], Hiroshi Sugiyama[12], Kohji Fukunaga[13], Norifumi Shioda[1,2†]

Fragile X-related tremor/ataxia syndrome (FXTAS) is a neurodegenerative disease caused by CGG triplet repeat expansions in *FMR1*, which elicit repeat-associated non-AUG (RAN) translation and produce the toxic protein FMRpolyG. We show that FMRpolyG interacts with pathogenic CGG repeat-derived RNA G-quadruplexes (CGG-G4RNA), propagates cell to cell, and induces neuronal dysfunction. The FMRpolyG polyglycine domain has a prion-like property, preferentially binding to CGG-G4RNA. Treatment with 5-aminolevulinic acid, which is metabolized to protoporphyrin IX, inhibited RAN translation of FMRpolyG and CGG-G4RNA–induced FMRpolyG aggregation, ameliorating aberrant synaptic plasticity and behavior in FXTAS model mice. Thus, we present a novel therapeutic strategy to target G4RNA prionoids.

INTRODUCTION

Fragile X-related tremor/ataxia syndrome (FXTAS) is a neurodegenerative disease caused by the expansion of CGG repeats in the 5′ untranslated region (5′-UTR) of *FMR1* (*1*). FXTAS clinically presents with intention tremor, cerebellar gait ataxia, parkinsonism, and cognitive decline (*2*). It is estimated that 1 in 403 men and 1 in 209 women have 55 to 200 CGG repeats and might be "premutation carriers"; of these, 40% men and 16% women will be diagnosed with FXTAS (*2*). The prevalence of FXTAS increases with age via unknown mechanisms (*3*).

Two major mechanisms have been proposed for FXTAS pathogenesis. One is "RNA gain of function"; in this mechanism, the expanded CGG repeat–derived RNA complex interacts with RNA binding proteins (RBPs), such as heterogeneous nuclear ribonucleoprotein (hnRNP) A2B1 (*4*), src-associated substrate during mitosis of 68 kDa (Sam68) (*5*), DiGeorge syndrome critical region gene 8 (DGCR8) (*6*), and TAR DNA binding protein of 43 kDa (TDP-43) (*7*), which sequestrate into inclusion bodies to form RNA foci. Aggregated RNA foci are a hallmark neuropathological indicator of FXTAS (*8*, *9*), indicating cellular dysfunction by rendering the sequestrated RBPs unavailable for other substrates, such as specific splicing defects (*4*, *5*, *10*).

The second pathogenic mechanism is "repeat-associated non-AUG (RAN) translation," wherein *FMR1* mRNA containing expanded CGG repeats initiates translation outside the traditional AUG start codon (*11*). RAN translation can occur with both sense and antisense strand CGG repeat mRNA transcripts in vitro (*12*, *13*). Of the RAN translation products, a polyglycine-containing protein, FMRpolyG, is critical for the formation of inclusions observed in the brains of patients with FXTAS (*14*). FMRpolyG has been identified in CGG knock-in (KI) mice (*11*, *15*), postmortem human FXTAS brains (*11*, *13*, *15*), and FXTAS peripheral tissues (*16*, *17*). A recent study suggested that the FMRpolyG C terminal region (Cterm) has a toxic effect in neuronal cells, which disorganizes the nuclear lamina architecture through interaction with the nuclear lamina-associated polypeptide 2β (*15*). However, a key question is whether FXTAS pathogenesis occurs through the expansion of CGG repeats as RNA gain-of-function, RAN translation, both, or neither. Here, we aimed to investigate this aspect and identify agents that can interrupt the pathogenic mechanism.

RESULTS

Liquid-to-liquid phase separation before liquid-to-solid transition in FMRpolyG

We first investigated the molecular motifs of poly(99)-glycine (polyglycine) in FMRpolyG using bioinformatics. The polyglycine region of FMRpolyG was predicted to have low-complexity disordered domains with RNA binding ability using the predictor of naturally disordered regions (PONDR) (*18*) method (Fig. 1A, blue) and prion-like domains (PrLDs) using the prion-like amino acid composition (PLAAC) (*19*) method (Fig. 1A, orange). Hydrophobic pattern analysis revealed that the Cterm had high hydrophobicity (ExPASy Molecular Biology Server) (Fig. 1A, green) (*20*).

Next, we examined whether FMRpolyG directly interacts with CGG repeat–derived RNA using an electrophoresis mobility shift

[1]Department of Genomic Neurology, Institute of Molecular Embryology and Genetics (IMEG), Kumamoto University, Kumamoto, Japan. [2]Graduate School of Pharmaceutical Sciences, Kumamoto University, Kumamoto, Japan. [3]Department of Neurology, Graduate School of Medical Sciences, Kumamoto University, Kumamoto, Japan. [4]Liaison Laboratory Research Promotion Center, Institute of Molecular Embryology and Genetics (IMEG), Kumamoto University, Kumamoto, Japan. [5]Division of Radioisotope Science, Research Initiative Center, Organization for Research Initiative and Promotion, Tottori University, Tottori, Japan. [6]Division of Genomic Science, Research Initiative Center, Organization for Research Initiative and Promotion, Tottori University, Tottori, Japan. [7]Department of Biomedical Science, Institute of Regenerative Medicine and Biofunction, Graduate School of Medical Science, Tottori University, Tottori, Japan. [8]Chromosome Engineering Research Center, Tottori University, Tottori, Japan. [9]Department of the Neurology, Division of Clinical Medicine, Faculty of Medicine, University of Tsukuba, Ibaraki, Japan. [10]Division of Neurology, Department of Medicine, Jichi Medical University, Shimono, Japan. [11]Office for Research Strategy, Organization for Research Initiative and Promotion, Tottori University, Tottori, Japan. [12]Department of Chemistry, Graduate School of Science, Kyoto University, Kyoto, Japan. [13]Department of Pharmacology, Graduate School of Pharmaceutical Sciences, Tohoku University, Sendai, Japan.
*These authors contributed equally to this work.
†Corresponding author. Email: shioda@kumamoto-u.ac.jp

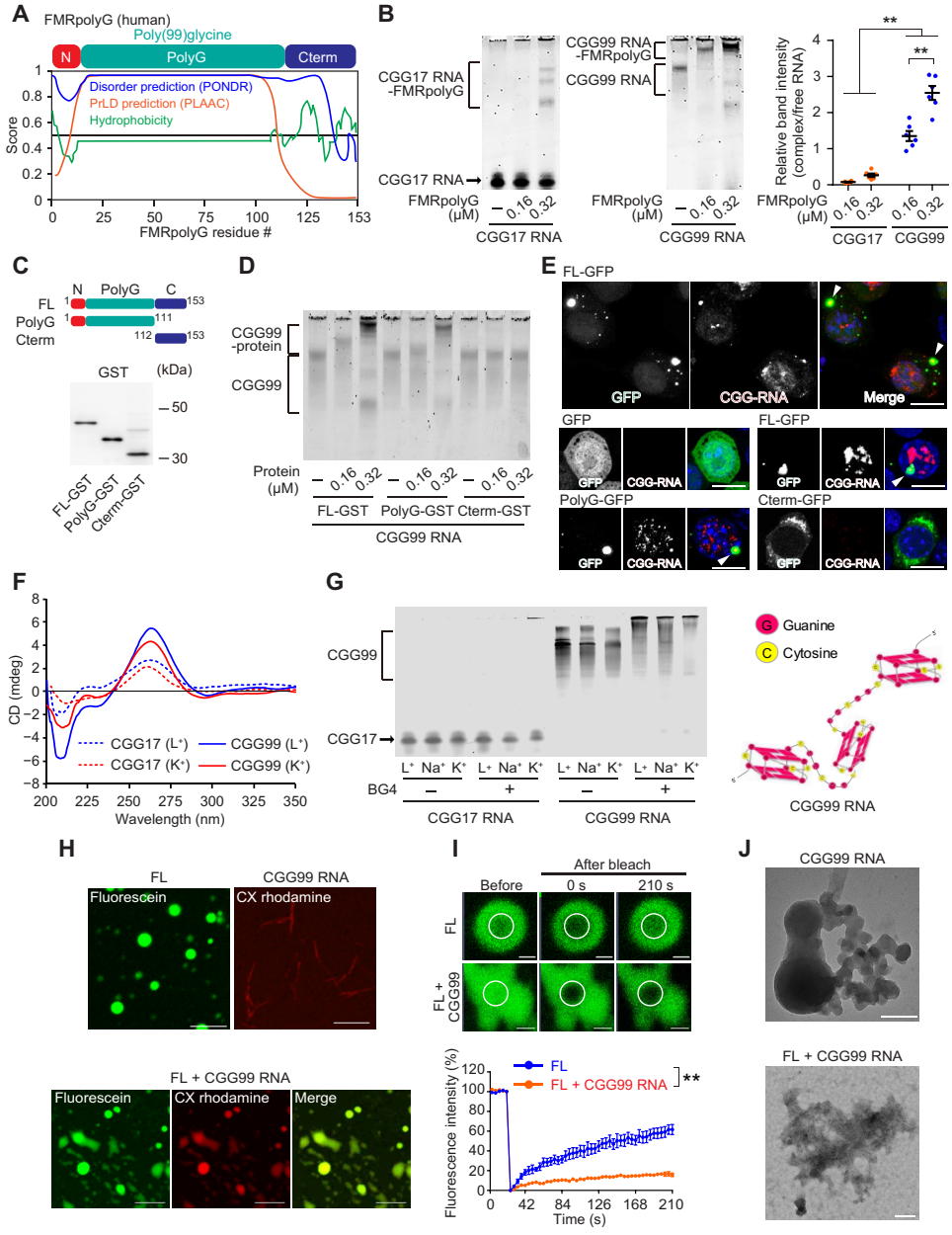

Fig. 1. FMRpolyG undergoes phase transition by CGG-G4RNA. (**A**) Bioinformatics analysis of FMRpolyG. Levels of protein disorder predicted by the PONDR (blue); prion-likeness, by the PLAAC (orange); and hydrophobicity, by ExPASy (green). (**B**) Representative EMSA for FMRpolyG proteins using CGG17 or CGG99 RNA (left); quantification of FMRpolyG-RNA complexes (right). $^{**}P < 0.01$. (**C**) Schematic representation of the constructs of the FMRpolyG mutant (top). Representative immunoblot data of GST-tagged FMRpolyG constructs using an anti-GST antibody (bottom). (**D**) Representative EMSA for GST-FMRpolyG mutant proteins using CGG99 RNA. (**E**) Confocal images show aggregated GFP-positive inclusions (green, arrowheads) colocalized with fluorescent in situ hybridization–labeled CGG-RNA (red) in Neuro-2a cells. Nuclear DNA was labeled with 4′,6-diamidino-2-phenylindole (DAPI) (blue). Scale bars, 5 μm. (**F**) Circular dichroism (CD) spectra of CGG17 and CGG99 RNA. (**G**) Representative EMSA with the BG4 antibody using CGG17 or CGG99 RNA (left). Pathogenic CGG99 RNA forms rigid secondary structures, including G4 (right). (**H**) Confocal images of phase-separated droplets formed by fluorescein-labeled FMRpolyG (FL, green) with or without CX rhodamine–labeled CGG99 RNA (red). Scale bars, 5 μm. (**I**) Fluorescence recovery after photobleaching experiments in fluorescein-labeled FMRpolyG (FL, green) without or with CGG99 RNA. $^{**}P < 0.01$. Scale bars, 0.5 μm (FL) and 1 μm (FL + CGG99). (**J**) Transmission electron microscopy images for CGG99 RNA (top) and FMRpolyG with CGG99 RNA (bottom). Scale bars, 100 nm. Source data are provided in table S3.

assay (EMSA) in normal range CGG17 RNA and pathogenic range CGG99 RNA. When purified glutathione *S*-transferase (GST)–tagged FMRpolyG with polyglycine (PolyG) was added to CGG repeat RNAs, FMRpolyG significantly and preferentially formed a complex with CGG99 RNA than with CGG17 RNA (Fig. 1B). To identify the domain that binds to CGG repeat RNAs, we performed EMSA in CGG repeat RNAs with GST-tagged FMRpolyG mutant proteins for amino acid 1 to 153 (full length; FL), amino acid 1 to 111 (PolyG), and amino acid 112 to 153 (Cterm) (Fig. 1C). Consistent with the prediction algorithms (Fig. 1A), the CGG repeat RNAs could bind to FL and PolyG but not to Cterm (Fig. 1D and fig. S1A). We confirmed GST-tagged FMRpolyG amino acid 13 to 111

[N terminus (N terminal region) deleted PolyG] could also bind CGG99 RNA (fig. S1B), suggesting that the polyglycine domain is critical for binding to CGG repeat RNAs, especially pathogenic range CGG99 RNA. In green fluorescent protein (GFP)–tagged FL- and PolyG-expressing cells, we observed strongly aggregated GFP-positive inclusions that colocalized with RNA foci labeled with a CCG8 antisense probe (Fig. 1E, arrowheads) and with transfected CX rhodamine–labeled CGG99 RNA (fig. S1C).

Although substantial biophysical and biochemical evidence has shown that short CGG repeat RNA oligoribonucleotides (<20 repeats) form hairpin or G-quadruplex (G4) structures (*21*), the folding structure in pathogenic CGG repeat RNA is unclear. To gain deeper insights into the secondary structures of pathogenic CGG repeat RNA, we measured the circular dichroism (CD) spectra in CGG99 RNA (Fig. 1F). In G4-nonstabilizing Li^+ conditions, positive and negative CD absorption bands at 262 and 210 nm were detected, which were characteristic of an A-form duplex RNA conformation. However, in G4-stabilizing K^+ conditions, a negative band at 210 nm was recovered toward the positive side, which is consistent with G4 conformation (*22*). In CGG17 RNA prepared with the same concentration as CGG99 RNA, CD measurements indicated lower absorptions at 262 and 210 nm compared with CGG99 RNA under Li^+ and K^+ conditions, showing a smaller proportion of rigid secondary structures than those of CGG99 RNA.

We next performed EMSA for CGG repeat RNAs using a G4-specific antibody (BG4) (Fig. 1G, left, and fig. S1D). The CGG99 RNA produced smeared bands, indicative of the formation of various higher-order structures, while the treatment with BG4 migrated these RNA bands upward under Li^+, Na^+, and K^+ conditions. By contrast, with CGG17 RNA, the efficiency of BG4-bound migration was much lower than that for CGG99 RNA, and CGG17 RNA was detected as a single band, which was detected only slightly in the K^+ condition. We confirmed that the GFP-positive inclusions colocalized with BG4-positive foci in GFP-tagged FL and PolyG-expressing cells (fig. S1E, arrowheads). Collectively, pathogenic CGG99 RNA had a greater opportunity to form rigid secondary structures, including G4, than CGG17 RNA did (Fig. 1G, right).

Proteins have PrLDs that drive their liquid-to-liquid phase separation (LLPS) and can reversibly form intracellular membrane-less droplets (*23*, *24*). Thus, we hypothesized that FMRpolyG may undergo LLPS. To test this hypothesis, we examined whether recombinant FMRpolyG mutants could form liquid-like droplets. As we expected, fluorescein-labeled FL and PolyG formed phase-separated droplets, but the Cterm construct did not (Fig. 1H and fig. S1F). The droplet formation of FL and PolyG disappeared by adding 1,6-hexanediol, which disrupts weak hydrophobic interactions between PrLDs (fig. S1F) (*25*). We found that CX rhodamine–labeled CGG99 RNA could form fibril-like assemblies on its own in the same phase separation condition, but CGG17 RNA did not (Fig. 1H and fig. S1F). We next investigated whether adding CGG99 RNA would influence the ability of FMRpolyG to undergo LLPS. Fluorescein-FL and PolyG could form droplets and colocalize with CX rhodamine–labeled CGG99 RNA (Fig. 1H and fig. S1G).

To characterize the dynamic nature of the droplets, we next performed fluorescence recovery after photobleaching (FRAP) experiments. FRAP studies revealed that fluorescence recovery of the bleached region of FL and PolyG droplets was very rapid at the beginning of their formation, significantly decreasing in the presence of CGG99 RNA (Fig. 1I and fig. S1H), suggesting that CGG99 RNA accelerates the transition of FMRpolyG from a liquid state to an aberrant gel-like state of aggregates. To investigate the importance of the G4RNA for liquid-to-solid transition in FMRpolyG, FRAP analysis of FMRpolyG was performed in the presence of a mutant telomeric repeat–containing RNA (mTERRA) that is unable to form G4 (fig. S1I). In the presence of mTERRA, the fluorescence recovery of the bleached region of FL droplets was showed rapid as same as FL alone, suggesting that the gel-like transition of FMRpolyG is accelerated by G4RNA. Neuro-2a cells overexpressing GFP-tagged FL had mobile intracellular droplets (arrows) and inclusion bodies that were strongly aggregated (arrowheads) (fig. S1J). FRAP of droplet-like foci revealed a fast recovery rate, while aggregated foci appeared less mobile (fig. S1I). We also confirmed the hydrogel states of CGG99 RNA and amorphous aggregates of FMRpolyG and CGG99 RNA by transmission electron microscopy (TEM) (Fig. 1J). These results suggested that the polyglycine region within FMRpolyG was essential for phase separation and that the CGG repeat–derived G4RNA (CGG-G4RNA) promoted the liquid-to-solid transition and aggregate formation of FMRpolyG.

Complex formation with RBPs and exosomal proteins

To identify the endogenous expression of FMRpolyG, we developed a monoclonal antibody (1C7) against its C-terminal peptide (Fig. 2A). We confirmed the specificity of 1C7 in Neuro-2a cells expressing FLAG-tagged FMRpolyG with the polyglycine domain by immunoblotting. Both 1C7 and a FLAG antibody recognized a protein band at 15 kDa (Fig. 2B, left). The 1C7 antibody could also recognize endogenous FMRpolyG in the hippocampal lysate of CGG-KI but not in age-matched wild-type (WT) mice (Fig. 2B, right). In CGG-KI hippocampal slices, the 1C7 antibody labeled FMRpolyG in cytoplasmic and nuclear granules (Fig. 2C), which were ubiquitin-positive (Fig. 2D). In addition, FMRpolyG colocalized with RNA foci labeled with a CCG8 antisense probe in CGG-KI hippocampal cells (fig. S2A). FMRpolyG and CCG8-labeled RNA foci colocalized with BG4 antibody-labeled G4 foci, which are significantly larger compared to the other G4 foci in CGG-KI hippocampal cells, respectively (fig. S2, B and C). We confirmed that BG4 immunoreactivities were disappeared in the presence of ribonuclease A (RNase A) in WT and CGG-KI hippocampal cells (fig. S2D). Endogenous FMRpolyG foci were detected in NeuN-positive neurons and glial fibrillary acidic protein (GFAP)–positive astrocytes (fig. S2E).

To determine FMRpolyG-interacting proteins, we performed shotgun liquid chromatography coupled with tandem mass spectrometry (LC-MS/MS) on pull-down samples from CGG-KI hippocampal lysates using the 1C7 antibody. In total, 46 proteins that were potentially components of an endogenous FMRpolyG complex were identified (Fig. 2E and table S1). Notably, 39 proteins were included in the exosomal proteins present in the ExoCarta database (*26*), and 18 were annotated as RBPs [Gene Ontology (GO): 0003723] in the GO database. Furthermore, when we compared these proteins, 17 proteins overlapped, including hnRNP A2B1, which is a component of pathological inclusions observed in the brains of patients with FXTAS (*10*).

We used an immunoprecipitation assay to examine the interaction of FMRpolyG with hnRNP A2B1 and the exosomal proteins peptidylprolyl isomerase A (PPIA), eukaryotic translation elongation factor 1 alpha 1 (eEF1A1), and pyruvate kinase M1/2 (PKM) from the top 100 proteins in the ExoCarta database (*26*) in vivo. These proteins coprecipitated with FMRpolyG immunoprecipitated from

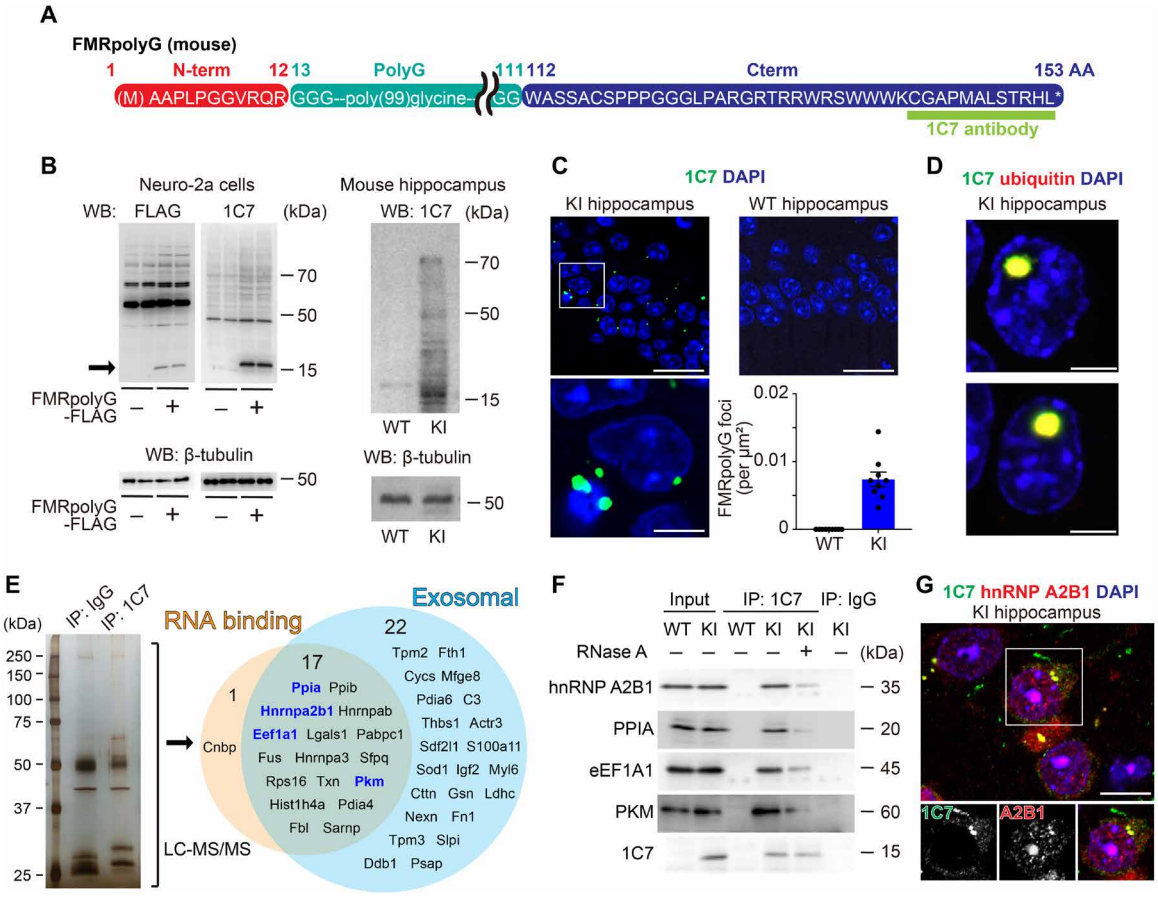

Fig. 2. FMRpolyG forms a complex with RBPs and exosomal proteins via RNAs. (**A**) Schematic representation of the epitope of 1C7 antibody (green) in FMRpolyG. AA, amino acid. (**B**) Immunoblotting using 1C7 and FLAG antibodies in Neuro-2a cells transfected with mock or FMRpolyG-FLAG. The arrow indicates the band corresponding to FMRpolyG-FLAG (left). 1C7 antibody in hippocampal lysates from WT or CGG-KI (KI) mouse (right). WB, Western blot. (**C**) Representative confocal images of FMRpolyG foci in the hippocampus of CGG-KI (left) and WT (right) mouse. The graph represents the number of FMRpolyG foci/μm^2; $n = 9$ mice each. Magnification of the white box in the upper left (bottom left). Scale bars, 20 μm (top) and 5 μm (bottom). (**D**) Representative confocal images showing the colocalization of FMRpolyG with ubiquitin in the hippocampus of CGG-KI mice. Scale bars, 5 μm. (**E**) LC-MS/MS shotgun analysis of pull-down samples from CGG-KI hippocampal lysates using the 1C7 antibody. Silver-stained SDS–polyacrylamide gel electrophoresis gel of eluates with mouse IgG or 1C7 antibodies (left). The annotations identified in the analysis (right). The proteins shown in blue were investigated in this study. IP, immunoprecipitation. (**F**) Immunoprecipitation assay with the 1C7 antibody from hippocampal lysates. Aliquots of extracts (1% input) and eluates were immunoblotted with the indicated antibodies. (**G**) Representative confocal images showing the colocalization of FMRpolyG foci with hnRNP A2B1 in the hippocampus from CGG-KI mouse. Magnification of the white box in the upper panel (bottom). Scale bar, 10 μm. Source data are provided in table S3.

CGG-KI hippocampal lysates but not from WT lysates (Fig. 2F). Furthermore, treatment with RNase A markedly reduced their interactions, suggesting that these complexes were dependent on the presence of RNAs (Fig. 2F). We also confirmed that FMRpolyG foci colocalized with hnRNP A2B1-positive foci in CGG-KI hippocampal cells (Fig. 2G).

FMRpolyG and neuronal dysfunction

Since FMRpolyG primarily interacted with exosomal proteins (Fig. 2E), we asked whether FMRpolyG was contained in exosomes. We isolated the exosome-containing fraction from the conditioned medium of mouse primary cortical cultured neurons by high-speed centrifugation (Fig. 3A, left) and performed ultrastructural analysis on this fraction using electron microscopy. We observed cup-shaped vesicles (arrowheads) with diameters of 30 to 200 nm, consistent with exosomes. There were no differences in the size distribution between the exosomes from WT- and CGG-KI–cultured neurons (Fig. 3A, right). We confirmed by immunoblot analysis that the isolated fraction contained exosomes using the markers PPIA, eEF1A1, and PKM, as well as hnRNP A2B1, whereas the Golgi apparatus marker GM130 was absent. FMRpolyG was detected in the exosome-containing fraction from cultured neurons of CGG-KI mice (Fig. 3B). FMRpolyG was observed in the exosomes from cultured neurons of CGG-KI mice by electron microscopy using immunogold labeling with the 1C7 antibody (Fig. 3C).

Many neuropathogenic proteins—e.g., Tau, α-synuclein, and TDP-43—undergo cell-to-cell transmission via exosomes (*27*). To examine whether FMRpolyG-carrying exosomes were absorbed by intact cells, primary cultured neurons from WT mice were incubated with PKH26-labeled exosomes purified from either CGG-KI– or WT-cultured neurons. As expected, strong FMRpolyG immunoreactivity was observed in all recipient neurons treated with CGG-KI exosomes after 24 hours but not in cells treated with WT exosomes (Fig. 3D and fig. S3A).

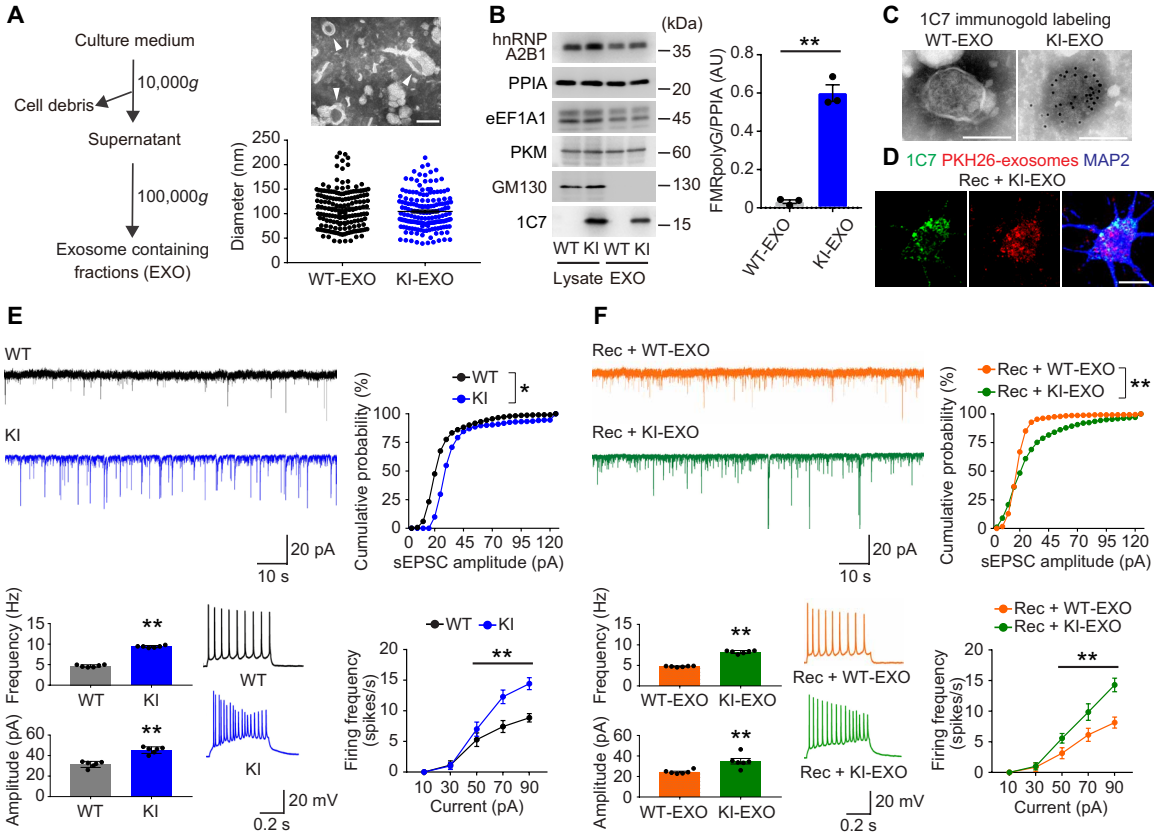

Fig. 3. FMRpolyG can propagate via exosomes, eliciting neuronal dysfunction. (**A**) The exosome-containing fraction (EXO) was isolated from primary cultured neurons using sequential centrifugation (left). Exosomes isolated by centrifugation were imaged to evaluate their morphologies (indicated by arrowheads; right). The size distribution of these exosomes from WT and CGG-KI (KI) neurons was measured by electron microscopy ($n = 165$ particles analyzed from each group). Scale bar, 100 nm. (**B**) Whole-cell lysates and EXO were subjected to Western blotting with antibodies against the indicated proteins. The experiments were repeated thrice, with similar results (left). Protein content was measured using densitometric analysis of FMRpolyG normalized to PPIA (AU, arbitrary units). $^{**}P < 0.01$; $n = 3$ each (right). (**C**) Immunogold labeling experiments using the 1C7 antibody detected FMRpolyG in the exosomes from CGG-KI (KI-EXO) but not WT (WT-EXO) primary cultured neurons. Scale bar, 100 nm. (**D**) Representative confocal images of FMRpolyG (green), PKH26-exosomes (red), and MAP2 (blue) in recipient neurons (Rec) treated with KI-EXO after 24 hours. Scale bar, 10 μm. (**E** and **F**) Amplitude and frequency of spontaneous excitatory postsynaptic currents (sEPSCs) and firing frequency in primary neurons from WT and CGG-KI mice (E) and in recipient neurons (Rec) treated with WT-EXO and KI-EXO (F). $^{**}P < 0.01$ and $^{*}P < 0.05$; $n = 6$ cells from three mice each. Source data are provided in table S3.

Next, we investigated whether CGG-KI exosome recipient neurons showed changes in neuronal function using electrophysiological analysis. Consistent with previous electrophysiological studies in primary cultured neurons from CGG-KI mice (*28*, *29*), the amplitude and frequency in spontaneous excitatory postsynaptic currents (sEPSCs) and the firing frequency significantly increased in CGG-KI compared with WT cultured donor neurons (Fig. 3E). In recipient neurons treated with CGG-KI exosomes, the amplitude and frequency in sEPSCs markedly increased compared with WT exosome-treated neurons. Current steps of equal intensity also produced a higher number of spikes in CGG-KI exosome-treated neurons than in WT exosome-treated neurons (Fig. 3F).

To investigate the sorting domain of FMRpolyG into exosomes, we purified exosomes from the supernatant of Neuro-2a cells transfected with various 3xFLAG-tagged FMRpolyG constructs; FL-FLAG, PolyG-FLAG, and Cterm-FLAG were used for immunoblot analysis. FL-FLAG and PolyG-FLAG but not Cterm-FLAG were detected in the exosome-containing fraction (fig. S3B). FLAG immunoreactivity was observed in recipient neurons treated with FL-FLAG and PolyG-FLAG exosomes, after 24-hour incubation, but this FLAG signal was not observed in cells that received Cterm-FLAG exosomes (fig. S3C). Electrophysiological abnormalities were observed in FL-FLAG– and PolyG-FLAG–expressing neurons compared with pcDNA3.1 vector-only (mock) cells; prominent effects were also observed in Cterm-FLAG–expressing neurons (fig. S3D). The application of exosomes from FL-FLAG– and PolyG-FLAG–expressing cells to recipient neurons significantly increased the amplitude and frequency of sEPSCs and firing rate compared with those of mock and Cterm-FLAG–expressing cells (fig. S3E). These results suggested that the polyglycine domain is required for the sorting of FMRpolyG into exosomes.

Inhibition of LLPS and RAN translation of FMRpolyG by PpIX

We previously discovered a novel G4-binding agent 5-aminolevulinic acid (5-ALA), which produces porphyrins protoporphyrin IX (PpIX) and hemin in cells (*30*, *31*). Therefore, by measuring the spectral transition of porphyrins, we examined whether PpIX and/or hemin could interact with CGG-G4RNA. Optical properties in hyperchromicity and long-wavelength shifts after RNA addition were quantified by monitoring the Soret band derived from porphyrin (*32*).

When PpIX was added to CGG7 and CGG17 RNA, little hyperchromicity was observed, whereas pronounced hyperchromicity was observed in a dose-dependent fashion when PpIX was added to CGG99 RNA (Fig. 4A). We also observed a greater shift of the Soret band to the long-wavelength side upon the addition of PpIX and CGG99 RNA when compared with CGG7 and CGG17 RNA (Fig. 4A). By contrast, hemin yielded the opposite binding status, exhibited by a higher hyperchromicity and long-wavelength shift upon CGG7 RNA and CGG17 RNA addition compared with CGG99 RNA addition (fig. S4A). To further confirm the repeat length-dependent interaction

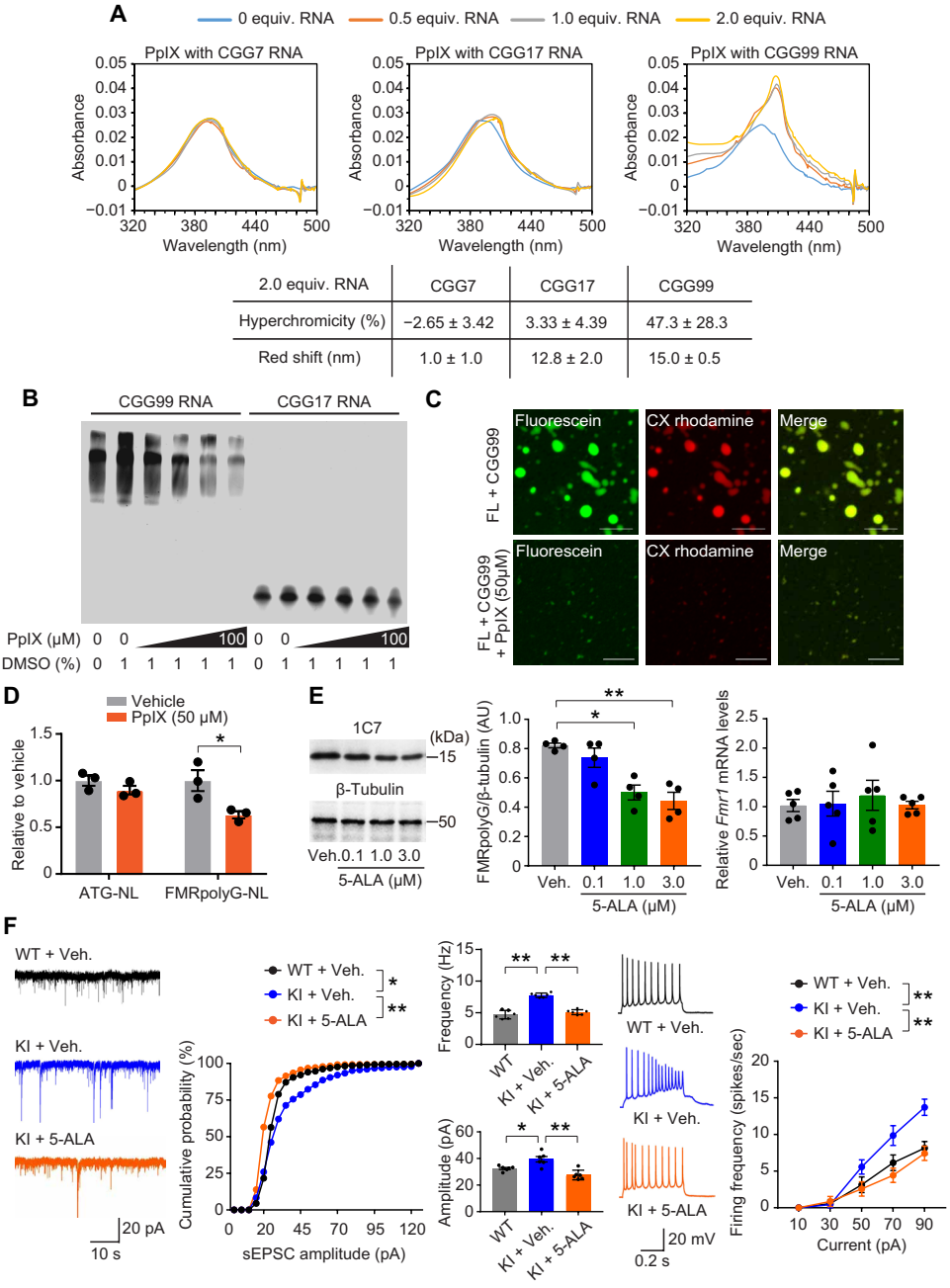

2.0 equiv. RNA	CGG7	CGG17	CGG99
Hyperchromicity (%)	−2.65 ± 3.42	3.33 ± 4.39	47.3 ± 28.3
Red shift (nm)	1.0 ± 1.0	12.8 ± 2.0	15.0 ± 0.5

Fig. 4. 5-ALA metabolite PpIX inhibits LLPS-derived FMRpolyG aggregation and RAN translation by binding to CGG-G4RNA. (**A**) Representative ultraviolet-visible spectra of PpIX upon CGG repeat RNA addition (top). Hyperchromicity and long-wavelength shift with two equivalents of PpIX (bottom). Experiments were repeated thrice. (**B**) Representative EMSA of CGG17 and CGG99 RNA treated with PpIX (12.5, 25, 50, and 100 μM). Experiments were repeated thrice. DMSO, dimethyl sulfoxide. (**C**) Confocal images of phase-separated droplets formed by fluorescein-labeled FMRpolyG (FL, green) and CX rhodamine–labeled CGG99 RNA (red) without (top) or with (bottom) 50 μM PpIX. Scale bars, 5 μm. (**D**) PpIX inhibited RAN translation of FMRpolyG using an in vitro luciferase assay. $^{*}P < 0.05$; experiments were repeated thrice. (**E**) Representative immunoblot of CGG-KI primary neuron lysates probed with the indicated antibodies (left). Protein content was measured using densitometric analysis of FMRpolyG normalized to β-tubulin (AU, arbitrary units). $^{**}P < 0.01$, $^{*}P < 0.05$; $n = 4$ mice each (middle). Real-time RT-qPCR for *Fmr1* mRNA expression in the primary cortical neurons of CGG-KI mice; $n = 5$ mice each (right). (**F**) Amplitude and frequency in sEPSCs and firing frequency in CGG-KI primary neurons following 7 days of 3 μM 5-ALA treatment. $^{**}P < 0.01$ and $^{*}P < 0.05$; $n = 6$ cells from three mice each. Source data are provided in table S3.

between PpIX and CGG RNA, we performed an EMSA of CGG17 and CGG99 RNA treated with PpIX. The CGG99 RNA bands reduced as PpIX concentrations increased because of the quenching of fluorescent dye by the close proximity of PpIX that interacts with RNAs. However, the intensity of CGG17 RNA did not change following PpIX treatment (Fig. 4B), consistent with the observation that PpIX interacts with CGG99 RNA with a higher affinity than with CGG17 RNA. We next investigated whether PpIX affects the LLPS of FMRpolyG in vitro. The phase-separated liquid droplets and hydrogels of complexes of fluorescein-FMRpolyG and CX rhodamine–CGG99 formed substantially smaller droplets after PpIX treatment compared to untreated controls (Fig. 4C). There were no differences in the droplet formation of fluorescein-FMRpolyG with or without PpIX (fig. S4B).

PpIX is also a candidate agent used to inhibit RAN translation in high-throughput in vitro screening assays (*33*). We confirmed that PpIX inhibited RAN translation of FMRpolyG using an in vitro luciferase assay (Fig. 4D). Because PpIX is nonbioavailable, we next investigated whether 5-ALA treatment could alter FMRpolyG expression in neurons. We treated primary cultured neurons from CGG-KI mice with different concentrations of 5-ALA for 7 days and found that 5-ALA reduced FMRpolyG protein expression in a dose-dependent manner without affecting *Fmr1* mRNA levels (Fig. 4E). Consistent with these results, the amplitude and frequency in sEPSCs and firing rate were recovered in CGG-KI primary neurons following 5-ALA treatment (Fig. 4F).

Amelioration of learning and motor dysfunction by 5-ALA treatment

Oral administration of 5-ALA improved cognitive dysfunction caused by mutations in the G4-binding protein ATRX, which have been observed in an α-thalassemia intellectual disability X-linked syndrome mouse model and human patients (*30*, *31*). We previously confirmed that 5-ALA [3 mg/kg, p.o. (per os)] is nontoxic and can cross the blood-brain barrier (*30*). Accordingly, we administered 5-ALA (1 or 3 mg/kg, p.o.) daily for 1 month to 50- to 54-week-old CGG-KI mice and then assessed memory-related and motor behavior.

We observed no difference in spontaneous locomotor activity during a 48-hour period in any group (fig. S5A). To evaluate spatial memory in CGG-KI mice, we performed Y-maze and Barnes-maze tests. In the Y-maze test, impairment in CGG-KI mice was based on the percentage of alternation behaviors compared with WT mice, without changes in the total number of arm entries (Fig. 5A). 5-ALA administration significantly increased the percentage of spontaneous alternation behavior in CGG-KI mice in a dose-dependent manner (Fig. 5A). In the Barnes-maze test, the latency time to enter the target hole significantly decreased after four training days in WT mice, indicating normal improvement of cognitive performance (Fig. 5B). By contrast, the cognitive performance of CGG-KI mice showed significantly longer latency times than those seen in WT mice; however, 5-ALA administration significantly rescued this latency in CGG-KI mice (Fig. 5B). To examine motor coordination and balance, we performed a beam-walking test. The CGG-KI mice had a significantly higher number of foot slips compared with WT mice, and 5-ALA administration reduced the number of foot slips in CGG-KI mice in a dose-dependent manner (Fig. 5C).

We next administered 5-ALA (3 mg/kg) to CGG-KI mice and assessed electrophysiology, immunohistochemistry, and comprehensive gene expression using hippocampal tissues. Hippocampal long-term potentiation (LTP), which is critical for learning and memory, shows that CGG-KI mice have impaired hippocampal synaptic plasticity compared to WT mice (*34*). Consistent with this previous study, we observed reduced high-frequency stimulation (HFS)–induced LTP in CGG-KI mice compared with WT mice (Fig. 5D); this reduced LTP in CGG-KI mice was significantly restored following 5-ALA treatment (Fig. 5D). Furthermore, the number of FMRpolyG foci in the hippocampal CA1 region of CGG-KI mice was significantly reduced following 5-ALA treatment compared with untreated mice (Fig. 5E). PpIX increased the FMRP levels in the induced pluripotent stem cells (iPSC)–derived neurons from patients with fragile X syndrome (*35*). Furthermore, a recent study revealed that noncleaving antisense oligonucleotides that selectively block RAN translation of CGG repeats increased endogenous FMRP expression in human iPSC-derived neurons (*36*). Thus, we examined whether 5-ALA treatment restored FMRP expression while reducing the FMRpolyG expression in CGG-KI mouse hippocampus. FMRpolyG expression was markedly decreased in 5-ALA–treated CGG-KI relative to vehicle-treated CGG-KI mice. Moreover, reduced FMRP expression of vehicle-treated CGG-KI mice was significantly rescued in 5-ALA–treated CGG-KI mice (Fig. 5F). To investigate changes in gene expression in response to CGG-KI expression and 5-ALA treatment, we performed RNA sequencing analysis on extracted mRNA from the hippocampi of WT and CGG-KI– or 5-ALA–treated CGG-KI mice. In the hippocampal tissue of CGG-KI mice, limited changes in mRNA expression were observed; however, 5-ALA treatment of CGG-KI mice substantially blocked differential gene expression (fig. S5B and table S2).

DISCUSSION

In this study, we showed that CGG-G4RNA directly binds to the polyglycine region of FMRpolyG and promotes the formation of LLPS-derived FMRpolyG aggregates. Furthermore, FMRpolyG was sorted into exosomes, propagated cell-to-cell, and elicited neuronal dysfunction. From a pharmacological perspective, the formation of CGG-G4RNA–induced FMRpolyG aggregates was inhibited by the binding of PpIX to G4RNA. Moreover, RAN translation of FMRpolyG was also suppressed by PpIX. Oral administration of 5-ALA, which is converted into PpIX, suppressed FMRpolyG expression and significantly improved synaptic dysfunction and behavioral deficits in CGG-KI mice. CGG repeat RNA is related to two main molecular mechanisms in FXTAS pathogenesis: RNA gain of function and RAN translation. We showed that these two pathogenic mechanisms are not independent but instead mutually cause the formation of LLPS-derived FMRpolyG aggregates by CGG-G4RNA. Our findings suggest that FMRpolyG can form aggregates using CGG-G4RNA as a scaffold, which may act as an initial step toward FXTAS pathogenesis (Fig. 5G).

LLPS occurs when two liquid phases coexist in one system; it has been observed in membrane-less organelles and is responsible for the organization of many biochemical reactions and signaling complexes (*23*, *24*). Some RBPs with PrLDs undergo LLPS, where they function as scaffolds with distinctive short, linear motifs that participate in multiple interactions with other proteins and RNAs (*37*, *38*). In addition, RNAs also undergo LLPS to form RNA tandem repeats and homopolymers (*39*, *40*). Furthermore, the liquid-to-solid transition of LLPS could be due to the entanglement of biopolymers and/or the association of proteins and RNAs, leading to aggregations, as reported for many neuropathogenic proteins such as hnRNP A2B1, fused in sarcoma, and Tau (*38*, *41*–*44*).

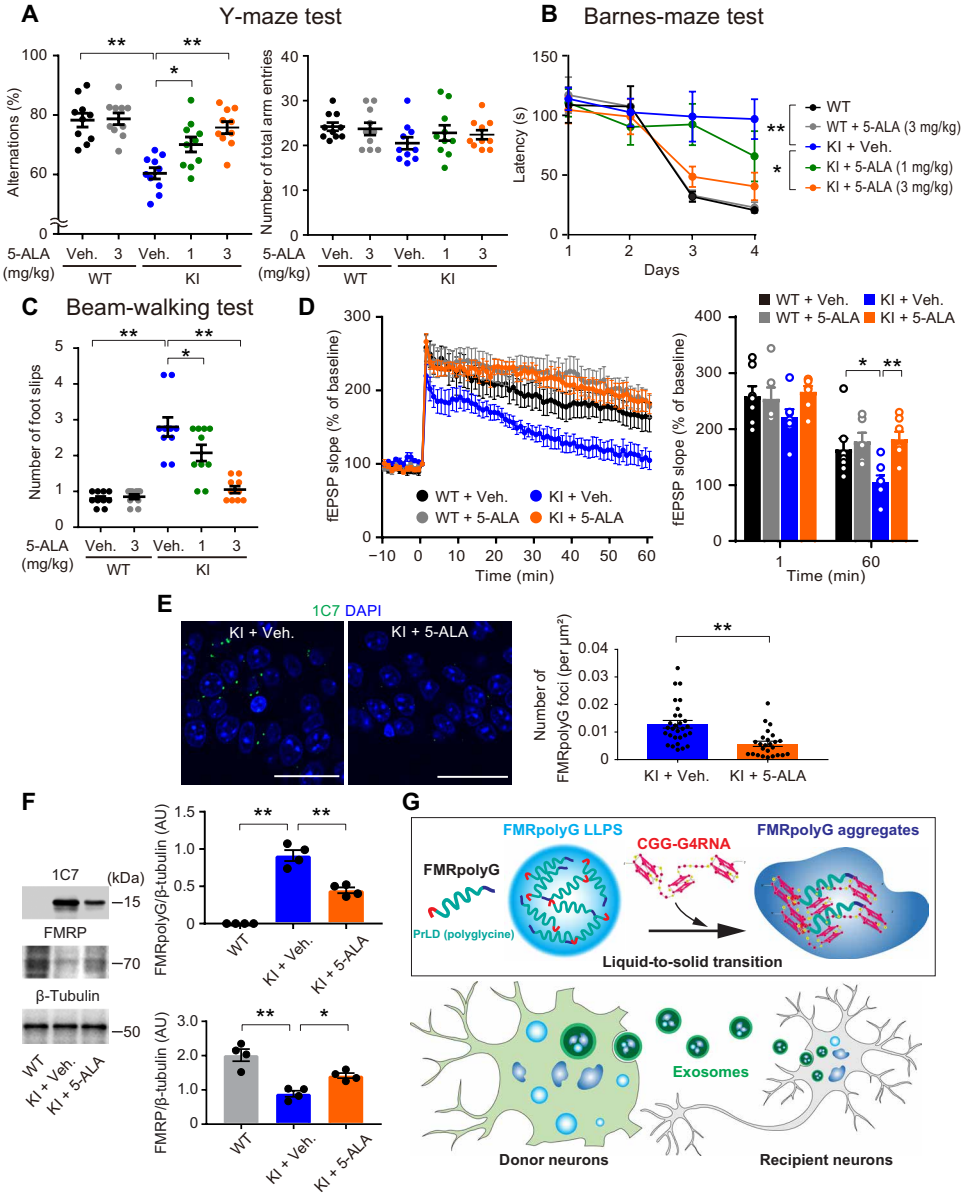

Fig. 5. Treatment with 5-ALA ameliorates learning and motor dysfunctions seen in CGG-KI mice. (**A** to **C**) 5-ALA treatment recovered learning and motor deficits in CGG-KI mice based on the Y-maze test (A), Barnes-maze test (B), and beam-walking test (C). $^{**}P < 0.01$, $^{*}P < 0.05$; $n = 10$ mice each. (**D**) Representative fEPSPs recorded from the hippocampal CA1 region (left). Changes in the fEPSP slope were recorded following HFS (middle). fEPSP slope changes following HFS at 1 or 60 min (right). $^{**}P < 0.01$, $^{*}P < 0.05$. WT + vehicle, CGG-KI + vehicle, and CGG-KI + 5-ALA: $n = 7$ mice; WT + 5-ALA: $n = 6$ mice. (**E**) Representative confocal images of intracellular aggregates in the hippocampal CA1 region of CGG-KI and 5-ALA–treated CGG-KI mice (top) and quantification of FMRpolyG aggregates (bottom). The graphs represent the number of FMRpolyG foci/μm^2. $^{**}P < 0.01$. CGG-KI + vehicle, $n = 6$ mice; CGG-KI + 5-ALA, $n = 5$ mice. Five hippocampal slices per mouse. Scale bars, 20 μm. (**F**) Protein content was measured using densitometric analysis of FMRpolyG and FMRP normalized to β-tubulin (arbitrary units). $^{**}P < 0.01$ and $^{*}P < 0.05$; $n = 4$ mice each. (**G**) CGG-G4RNA binds to the polyglycine region of FMRpolyG, promoting liquid-to-solid transition and aggregation of FMRpolyG via LLPS. FMRpolyG propagated cell-to-cell through exosomes, eliciting neuronal dysfunction. Source data are provided in table S3.

Here, we showed that the polyglycine region of FMRpolyG is a PrLD with low complexity that drives LLPS. This type of low complexity shows a strong sequence similarity to yeast prions enriched in polar uncharged amino acids (e.g., asparagine, glutamine, tyrosine, and glycine) (*45*). Furthermore, FMRpolyG droplets undergo a liquid-to-solid transition in the presence of CGG-G4RNA and transform into aggregates. We found that CGG-G4RNA itself could produce solid-like aggregates, suggesting that CGG-G4RNA serves as a nucleation center for the subsequent seed-dependent aggregations of RBPs with PrLDs. Recently, noncoding CGG repeat expansions in the 5′-UTR of *NOTCH2NLC*, *LOC642361/NUTM2B-AS1*, and *LRP12* were shown to cause neuronal intranuclear inclusion disease (NIID) and mimic FXTAS based on their clinical and neuroimaging manifestations (*46*, *47*). Clinical evidence of diseases caused by CGG repeat expansions indicates a possibility that CGG-G4RNA–derived RBP aggregation might be a molecular basis of NIID onset.

Many studies have reported neuronal dysfunctions through the cell-to-cell transmission of aggregated proteins, such as Tau and α-synuclein (*48*, *49*). These secreted proteins that are related to neurological disorders are released from affected donor cells and are transmitted to the recipient cells, where they act as templates to induce the normal endogenous counterpart protein to misfold, leading to the amplification of pathogenic protein conformation (*27*). The secretion of these pathogenic proteins into the extracellular space can occur through multiple pathways, namely, via the secretion of exosomes, through tunneling nanotubes and hemichannels between cells, and via the exocytosis of proteins (*27*). RBPs with PrLDs in a mammalian system that are similar to yeast prion domains appear to be frequent constituents of exosomes (*50*). Of the human RBPs with PrLDs, 71% have been reported in exosomal fractions that are sorted into exosomes with RNAs (*51*). For example, SUMOylated hnRNP A2B1 controls the sorting of microRNAs into exosomes (*52*), indicating that RBPs with PrLDs can be actively involved in the sorting of RNAs into exosomes. A study using a transgenic mouse line selectively expressing a CGG99 repeat linked to a GFP reporter in astroglia (Gfa2-CGG99 mouse) showed FMRpolyG expression in both neurons and astrocytes, which indicated the cell-to-cell propagation of FMRpolyG (*53*). In our study, FMRpolyG was sorted into exosomes via its polyglycine domain, and FMRpolyG-containing exosomes elicited neuronal dysfunctions in recipient cells. These results suggested that exosomes could mediate FMRpolyG propagation in FXTAS. However, we could not demonstrate whether FMRpolyG aggregates induced the misfolding of the native protein. Further examination will be required to reveal the involvement of FMRpolyG propagation in FXTAS pathogenesis.

We found that PpIX inhibited the RAN translation of FMRpolyG and CGG-G4RNA–induced FMRpolyG aggregation. A recent study revealed that G4RNA within an upstream open reading frame (uORF) at 5′-UTR stimulates translation initiation at the alternative translation initiation site and hinders the translation of the main downstream coding sequence (CDS). Furthermore, G4RNA folding within uORF stimulates 5′-UTR translation by pausing translating ribosomes and inducing a queue of ribosomes stretching back to the uORF start codons (*54*). Our data suggest that PpIX may unfold G4RNA within CGG repeats from *Fmr1* transcripts, thereby inhibiting RAN translation initiation at an ACG start codon located upstream of the repeats (*15*). In addition, the inhibition of ribosome queuing on the uORF start codon by PpIX may lead to increased translation of the downstream CDS. G4RNA folding/unfolding within CGG repeats may contribute to FMRP production. We also showed that the phase-separated hydrogels of complexes of FMRpolyG and CGG-G4RNA formed substantially smaller droplets after PpIX treatment compared to untreated controls. Thus, PpIX may unfold CGG-G4RNA, a scaffold for phase transition processes, thereby reducing FMRpolyG binding to CGG-G4RNA and the phase transition.

Although many G4-binding molecules, including porphyrins, are reported, none of these compounds have been shown to be bioavailable and safe, except for 5-ALA (*55*). The dysregulation of G4s by the expansion of G-rich sequences has been observed in a large hexanucleotide GGGGCC repeat with >1000 expansions in *C9orf72*-mediated amyotrophic lateral sclerosis and frontotemporal dementia (C9ALS/FTD) (*56*, *57*). Despite differences in the repeat sequences, RAN translation in FXTAS and C9ALS/FTD shares common mechanisms (*33*). Building on previous reports, we show that 5-ALA is a novel candidate agent for targeting G4-related neurological disorders by inhibiting RAN translation and G4RNA/RBP aggregation.

In conclusion, FMRpolyG undergoes LLPS, liquid-to-solid transition, and aggregation by CGG-G4RNA. FMRpolyG propagates from cell-to-cell through exosomes, thereby eliciting neuronal dysfunction. PpIX pharmacologically reduces FMRpolyG translation and FMRpolyG aggregation by affecting the binding ability of CGG-G4RNA. 5-ALA is converted into PpIX, which blocked FMRpolyG expression and ameliorated aberrant neuronal phenotypes in a FXTAS mouse model. Our findings suggest a novel therapeutic strategy to target CGG-G4RNA in FXTAS pathology.

MATERIALS AND METHODS

Animals

We used 50- to 54-week-old male CGG-KI mice and WT littermates. CGG-KI mice (*58*) were provided by R. Willemsen (Erasmus MC Rotterdam, The Netherlands). Male CGG-KI mice harbored 120 to 150 CGG repeats and were genotyped for CGG-repeat lengths as previously described (*59*). Mice were housed under climate-controlled conditions in a 12-hour light/12-hour dark cycle and were provided standard food and water ad libitum. Animal studies were conducted in accordance with the Kumamoto University institutional guidelines. Ethical approval was obtained from the Institutional Animal Care and Use Committee of the Kumamoto University Environmental and Safety Committee.

Cell culture

The Neuro-2a mouse neuroblastoma cell line CCL-131 was authenticated by the provider using short tandem repeat profiling (American Type Culture Collection) and were grown in Dulbecco's modified Eagle's medium supplemented with 10% exosome-depleted fetal bovine serum (FBS) and penicillin/streptomycin in a 5% CO_2 incubator at 37°C. FBS was centrifuged at 100,000*g* for 16 hours at 4°C, and the supernatant was carefully collected to remove exosomes. Cells were routinely tested for mycoplasma contamination. Transfection was performed using the Lipofectamine 2000 (Invitrogen) transfection reagent according to the manufacturer's protocol. Primary cultures of neurons were established using previously described methods (*30*). Briefly, cortical tissue was dissected from 18-day-old embryonic mice and dissociated with trypsin treatment and trituration through a Pasteur pipette. Neurons were plated on coverslips coated with poly-L-lysine in minimum essential medium (Invitrogen) supplemented with 10% exosome-depleted FBS, 0.6% glucose (Wako), and 1 mM pyruvate (Sigma-Aldrich). After cell attachment, coverslips were transferred to dishes containing a glial cell monolayer and maintained in neurobasal medium (Invitrogen) containing 2% B27 supplement (Invitrogen) and 1% GlutaMAX (Invitrogen). To inhibit glial proliferation, 5 μM cytosine β-D-arabinofuranoside (Sigma-Aldrich) was added to cultures at 3 days in vitro (DIV3). Cortical neurons were harvested at DIV21.

Plasmid constructs

The 5′-UTR–CGG×99-FMR1-EGFP (FMRpolyG-GFP, also termed as FL-GFP) plasmid was obtained from Addgene (number 63091). FMRpolyG-FLAG, PolyG-FLAG, PolyG-GFP, Cterm-FLAG, and Cterm-GFP were generated using the KOD-Plus Mutagenesis Kit (Toyobo) following the manufacturer's protocol. GST-fused plasmids (e.g., FL-GST, PolyG-GST, and Cterm-GST) were inserted

into pEX-C-GST (OriGene) using the in-fusion polymerase chain reaction (PCR) cloning system (Clontech) according to the manufacturer's protocol. The +1 (polyG) reading frames with nanoLuc fusion (FMRpolyG-NL) and ATG-NL plasmids were provided by P. K. Todd (University of Michigan Medical School, USA) (*12*).

Antibodies

The following primary antibodies were used in this study: anti-FMRpolyG 1C7 (1:5000; generated commercially, Sigma-Aldrich) against the CGAPMALSTRHL peptide, anti-GFP (1:1000; ab290, Abcam), anti-FLAG (1:1000; clone M2, F1804, Sigma-Aldrich), anti-DYKDDDDK tag (1:800; 14793S, Cell Signaling Technology), anti–β-tubulin (1:5000; clone AC-15, A5441, Sigma-Aldrich), BG4 (1:800, 1.0 μg/ml) (*60*), anti-hnRNP A2B1 (1:1000; ab31645, Abcam), anti-PPIA (1:500; 10720-1-AP, Proteintech), anti-eEF1A1 (1:500; 11402-1-AP, Proteintech), anti-PKM (1:500; 10078-2-AP, Proteintech), anti-GM130 (1:200; clone 35/GM130, 610822, BD Transduction Laboratories), anti-NeuN (1:1000; 26975-1-AP, Proteintech), anti-GFAP (1:1000; 23935-1-AP, Proteintech), anti-MAP2 (1:10,000; ab92434, Abcam), anti-ubiquitin (1:1000; ZO458, Dako), anti-FMRP (1:1000; clone 1C3; MAB2160, Millipore), and anti-GST (1:1000; MA4004, Invitrogen). For immunoblotting, the following secondary antibodies were used: horseradish peroxidase (HRP)–conjugated anti-mouse immunoglobulin G (IgG) antibody (1:5000; 1031-05, SouthernBiotech) and HRP-conjugated anti-rabbit IgG antibody (1:5000; 4050-05, SouthernBiotech). For immunocytochemistry and immunohistochemistry, the following secondary antibodies were used: Alexa 488–conjugated donkey anti-rabbit (1:500; A-21206, Invitrogen), Alexa 594–conjugated donkey anti-rabbit (1:500; A-21207, Invitrogen), Alexa 488–conjugated donkey anti-mouse (1:500; A-21202, Invitrogen), Alexa 594–conjugated donkey anti-mouse (1:500; A-21203, Invitrogen), and DyLight 405-AffiniPure donkey anti-chicken IgY (1:500; 703-475-155, Jackson ImmunoResearch).

Identification of FMRpolyG-interacting proteins by MS

Hippocampal tissues from 52-month-old CGG-KI mice were lysed in a buffer containing 50 mM tris-HCl (pH 7.5), 0.15 M NaCl, 0.1% Triton X-100, 4 mM EDTA, 4 mM EGTA, 1 mM Na_3VO_4, 50 mM NaF, 1 mM dithiothreitol, and protease inhibitors (trypsin inhibitor, pepstatin A, and leupeptin) and centrifuged at 15,000*g* for 10 min. Supernatants were collected and incubated on a Protein A Sepharose column (Protein A HP SpinTrap, GE Healthcare Life Sciences) with Tris Buffered Saline (TBS) buffer [50 mM tris-HCl and 0.15 M NaCl (pH 7.5)] containing 10 μg of 1C7 antibody at 4°C for 4 hours with constant rotation. The bound proteins were then washed with TBS and eluted with 2.5% acetic acid. To confirm specific binding, samples were separated by SDS–polyacrylamide gel electrophoresis (SDS-PAGE), and the gel was stained using a silver stain kit (Wako). LC-MS/MS analysis of all samples was outsourced to Oncomics. Proteins identified in control samples that were pulled down with 10 μg of mouse IgG were subtracted from the identified proteins.

Preparation of recombinant proteins

GST-tagged recombinant proteins were expressed in the *Escherichia coli* BL21 (DE3) strain (Novagen) cultured in Luria broth medium in the presence of ampicillin (100 mg/liter). The bacterial cultures were grown at 37°C to an approximate optical density of OD_{600} (optical density at 600) of 0.8. Protein expression was induced by the addition of isopropyl-β-D-thiogalactopyranoside (100 mg/liter), and the cultures were incubated at 20°C overnight. Bacterial cultures were harvested by centrifugation and lysed by sonication in buffer A [25 mM tris, 300 mM NaCl, and 5 mM β-mercaptoethanol (pH 7.5)] on ice. Lysates were then passed through a GST affinity column and eluted with a linear gradient of buffer A containing 10 mM glutathione. For the in vitro LLPS assay, the GST tag was removed in an overnight dialysis step at 4°C against a 4 liter of buffer [10 mM tris (pH 7.5), 150 mM NaCl, and 2 mM dithiothreitol] in the presence of tobacco etch virus protease.

Immunoprecipitation and immunoblotting

Immunoprecipitation and immunoblotting analyses were performed as previously described (*30*). Briefly, tissues or cells were homogenized in a buffer containing 50 mM tris-HCl (pH 7.5), 0.5% Triton X-100, 0.15 M NaCl, 4 mM EDTA, 4 mM EGTA, 1 mM Na_3VO_4, 50 mM NaF, 1 mM dithiothreitol, and protease inhibitors (trypsin inhibitor, pepstatin A, and leupeptin). For immunoprecipitation, lysates were incubated for 2 hours at 4°C with the indicated antibodies on a Protein A Sepharose CL-4B column (GE Healthcare Life Sciences) in homogenization buffer. The immunoprecipitates were washed thrice with homogenization buffer; equivalent amounts of protein were separated with SDS-PAGE, and proteins were then transferred to an Immobilon polyvinylidene difluoride membrane. Membranes were blocked with Tris Buffered Saline with Tween®20 (TBST) solution [50 mM tris-HCl (pH 7.5), 150 mM NaCl, and 0.1% Tween 20] containing 5% fat-free milk powder for 1 hour at room temperature and then incubated overnight at 4°C with the indicated primary antibodies. The membranes were then washed and incubated with the appropriate HRP-conjugated secondary antibody diluted in TBST. Blots were developed using an ECL immunoblotting detection system (Amersham Biosciences). Immunoreactive bands were visualized using the luminescent image analyzer LAS-4000 (Fujifilm).

Immunocytochemistry and immunohistochemistry

Immunocytochemistry and immunohistochemistry were performed as previously described (*30*). Briefly, brain slices and cells were fixed in 4% paraformaldehyde in phosphate-buffered saline (PBS) and then treated with PBS containing 0.1% Triton X-100 for 10 min. Antigen retrieval treated with 0.1 mM sodium citrate (pH 8.0, 10 min at 80°C) was performed to detect ubiquitin. Samples were incubated overnight at 4°C with primary antibodies, washed in PBS, and incubated with the appropriate secondary antibodies. For G4 foci staining, fixed brain slices and cells were incubated with an antibody that recognized an anti-DYKDDDDK tag (1:800; 14793S, Cell Signaling Technology) present on BG4 (1:800, 1.0 μg/ml) (*60*), followed by a fluorochrome-labeled secondary antibody that bound to the FLAG epitope tag. Determination of the size of G4 foci was performed using ImageJ Software. To confirm if G4 foci is attributed to RNA, slices were incubated with RNase A (20 μg/ml) in RNase buffer [10 mM tris-HCl (pH 8.0), 1 mM EDTA, and 500 mM NaCl] for 30 min at room temperature. Nuclei were stained with 4′,6-diamidino-2-phenylindole (DAPI) (R37606; Thermo Fisher Scientific). The samples were mounted with VECTASHIELD (Vector Laboratories), and fluorescence images were analyzed by confocal laser scanning microscopy (LSM780, Carl Zeiss).

Fluorescent in situ hybridization

Fixed brain slices and cells were washed with 1× diethylpyrocarbonate-treated PBS (DPEC-PBS) thrice for 20 min each and then incubated

with 0.3% Triton-X in 1× DPEC-PBS for 20 min. After several washes, the slices and cells were blocked in hybridization solution (50% formamide, 10% dextran sulfate, and yeast transfer RNA (0.1 mg/ml) in 2× SSC (300 mM NaCl and 30 mM sodium citrate) for 1 hour at 37°C and then incubated with 1 nM Cy5-$(CCG)_8$ DNA probe in hybridization solution at 37°C overnight. After hybridization, samples were washed twice for 20 min each with 50% formamide in 2× SSC at 37°C and then washed twice for 20 min each with 2× SSC and 0.2× SSC at room temperature. Samples were rinsed with 1× PBS, incubated with 1% bovine serum albumin and 0.3% Triton-X in PBS (blocking solution) for 1 hour at room temperature, and then treated with a primary antibody diluted in blocking solution overnight at 4°C. Diluted secondary antibody was added, and the samples were incubated for 3 hours at room temperature. DAPI was used as a counterstain for visualizing nuclei. After mounting, immunofluorescent images of the samples were collected using a confocal laser-scanning microscope (LSM780, Carl Zeiss).

Electrophoretic mobility shift assay

CGG17 or CGG99 RNA was prepared using an in vitro transcription T7 kit (Takara) or the HiScribe T7 Quick High Yield RNA Synthesis Kit (BioLabs) following the manufacturer's instructions, respectively. The RNAs were dissolved in 10 mM tris-HCl buffers (pH 7.5) containing 100 mM LiCl, NaCl, or KCl and were refolded by a heating/cooling process (90°C for 3 min, followed by cooling down to 10°C for 1.5 hours). The mixture was incubated with proteins at specified concentrations for more than 30 min at room temperature. For PpIX treatment, PpIX was added to the RNA solution before the heating/cooling process. The resultant samples were electrophoresed in a 6% polyacrylamide gel in 1× tris-borate EDTA running buffer (100 V, 90 min). The gels were stained with SYBR gold and visualized with Typhoon Trio equipment (GE Healthcare).

UV-vis spectral assays

One micromolar PpIX or hemin was prepared in 200-μl 10 mM tris-HCl buffer (pH 7.5) containing 100 mM KCl. To the sample solutions, aliquots of the master solutions of CGG7, CGG17, or CGG99 RNA were added at the same repeat concentration, and the mixtures were subjected to a heating/cooling process (90°C for 3 min, followed by cooling down to 10°C for 1.5 hours). The ultraviolet-visible (UV-vis) spectra of PpIX or hemin in the resultant solutions were recorded at 25°C over a range of 320 to 500 nm using a spectrophotometer V-650 (JASCO) in a 1-cm path quartz cuvette. The values of hyperchromicity and long-wavelength shift upon two equivalents of porphyrins were calculated.

CD spectroscopy

A CGG17 or CGG99 RNA oligomer was prepared in 10 mM tris-HCl buffer (pH 7.5) containing 100 mM LiCl or KCl with the same concentration. The oligomers were then refolded by a heating/cooling process (90°C for 3 min, followed by cooling down to 10°C for 1.5 hours) before measurement. The CD spectra were recorded at room temperature over the range of 200 to 350 nm with a JASCO J-805LST spectrometer in a 3-mm path length quartz cuvette.

FRAP assays

For fluorescence detection, recombinant proteins (FL, polyG, and Cterm) were labeled with fluorescein using the Fluorescein Labeling Kit-NH_2 according to the manufacturer's instructions (Dojindo Molecular Technologies Inc.). CGG99 RNA was labeled with CX rhodamine using the Label IT Nucleic Acid Labeling Kit according to the manufacturer's instructions (Mirus Bio LLC). Recombinant proteins (9 μM; 8 μM nonlabeled proteins and 1 μM fluorescently labeled proteins) were prepared in 10 mM tris-HCl buffer (pH 7.5) containing 25 mM NaCl, 10 mM $MgCl_2$, and 12% (w/v) glycerol and were then incubated for 1 hour at 23°C. Then, 10% (w/v) 1,6-hexanediol (Sigma-Aldrich) was used to disturb weak interactions that drive LLPS. Fluorescently labeled CGG99 RNA or mTERRA (20 ng/μl) (5′-UUACCGUUACCGUUACCGUUACCG-3′) was prepared in the same buffer. For the preparation of protein/RNA complex solutions, prefolded RNAs with or without 50 μM PpIX were added to the protein solutions, which were then incubated for 1 hour at 23°C. The resultant solutions were covered with coverslips using a 0.12-mm spacer and sealed before measurement. Photobleaching was done with 100% laser power to 50% intensity using the bleaching program of the ZEN software on a Zeiss LSM780 machine. Time-lapse images were recorded every 5 s using a Zeiss Objective Plan-Apochromat 63×/1.4 oil DIC M27 for tracking photorecovery behavior.

Exosome isolation

Exosome isolation from cell culture media was performed according to a previously reported method (*61*) with slight modifications. Culture media of Neuro-2a cells and primary cortical neurons at DIV21 were harvested and spun at 10,000*g* for 10 min to remove cell debris. The supernatants were then centrifuged at 100,000*g* for 90 min. The final pellets were resuspended with 3% SDS sample buffer for whole-extract analysis. Fluorescence labeling of exosomes was performed using a PKH26 Red Fluorescent Cell Linker Kit (Sigma-Aldrich) according to the manufacturer's instructions.

TEM analysis

TEM images for CGG99 RNA and FMRpolyG were collected with a HT7700 system (Hitachi High-Tech Corporation, Tokyo, Japan) operating at 80 kV. A 10 μl of sample was applied to a carbon-coated colloid film coated on a copper mesh (400-mesh; Nisshin EM, Tokyo, Japan) and incubated for 5 min. After a brief wash with 5 μl of nuclease-free water, the sample was stained with 5 μl of 10% EM-stain solution (Nisshin EM) for 2 min, rinsed briefly with 5 μl of Milli-Q water, and air-dried overnight before imaging. For electron microscopy analysis of exosome-containing fractions, samples were fixed in 2% paraformaldehyde and adsorbed onto Formvar-coated nickel grids. The 1C7 antibody (1:1000) solution of 1% bovine serum albumin in PBS was applied to the grids for 2 hours at room temperature, followed by incubation with 10-nm nanogold anti-mouse IgG (1:100; Nanoprobes) for 1 hour at room temperature. Samples were postfixed with 2% glutaraldehyde. For negative staining, exosome grids were transferred to a 50-μl drop of 2% phosphotungstic acid solution (pH 7.0). The samples were observed with a TEM (JEM-1400Plus, JEOL Ltd., Tokyo, Japan) at 100 kV using a charge-coupled device camera (EM-14830RUBY2, JEOL Ltd.).

In vitro RAN translation

In vitro translation was performed as previously reported with some modification (*33*). Briefly, RNAs were transcribed in vitro by T7 RNA polymerase (BioLabs) using FMRpolyG-NL and ATG-NL linearized by Xba I. The transcribed RNAs were capped and polyadenylated using the Vaccinia Capping System (BioLabs) and *E. coli*

Poly(A) Polymerase (BioLabs), respectively. Then, 6 nM capped and polyadenylated mRNAs were translated in a 20-μl reaction at 30°C for 60 min using the Flexi Rabbit Reticulocyte Lysate System (Promega). The solutions contained 50% rabbit reticulocyte lysate, 10 μM amino acid mixture minus leucine, 10 μM amino acid mixture minus methionine, RNasin ribonuclease inhibitor (0.8 U/μl), and 1% dimethyl sulfoxide with or without PpIX and were supplemented with 100 mM KCl and 0.5 mM $Mg(OAc)_2$. Reactions were diluted, and the translation efficiency was quantified by measuring NL luminescence on a GloMax luminometer (Promega).

RT-qPCR analysis

Total RNA was purified from cells using the RNeasy Mini Kit (Qiagen) according to the manufacturer's protocol. The RNA was reverse-transcribed into single-stranded complementary DNA (cDNA) using an oligo(dT) primer (Promega) and Moloney murine leukemia virus reverse transcriptase (Invitrogen) and then used in reverse transcription PCR (RT-PCR) with gene-specific primers. RT–quantitative PCR (qPCR) was performed in 48-well plates (Mini Opticon Real-Time PCR system, Bio-Rad) using iQ SYBR Green 2X Supermix (Bio-Rad). Gene expression was assessed using the differences in normalized C*t* (cycle threshold) (ΔΔC*t*) method after normalization to *GAPDH* expression. Fold change was calculated by 2-ΔΔC*t*. The following primers were used for RT-qPCR: *Gapdh* (forward, 5′-TGTGTCCGTCGTGGATCTGA-3′; reverse, 5′-CACCACCTTCTTGATGTCATCATAC-3′) and *Fmr1* (forward, 5′-AGAGGAGGAGGCTTCAAAGG-3′; reverse, 5′-CTACGCTGTCTGGCTTTTCC-3′).

RNA sequencing analysis

Total RNA was extracted from hippocampal slices from WT and CGG-KI– and 5-ALA–treated CGG-KI mice using the RNeasy Mini Kit according to the manufacturer's instructions (Qiagen). The total RNAs were quantified with a Qubit fluorometer (Life Technology) and Bioanalyzer (Agilent). A 100-ng aliquot of total RNA was used to isolate mRNA and prepare cDNA libraries using the NEBNext Ultra II Directional RNA Library Prep Kit for Illumina (New England BioLabs). The cDNA libraries from the samples (n = 3 for each group) were sequenced on an Illumina NextSeq 500 with a single 75–base pair read. Base calling and demultiplexing were performed using BaseSpaceONSITE. The adapter sequence and low-quality ends were trimmed using Trim Galore! version 0.5.0. The remaining reads were aligned to the mouse genome (UCSC mm10) using STAR version 2.6.0a. Gene expression profiles for each sample were measured as TPM using RSEM version 1.3.1. The scatter plots were constructed in R version 3.6.2.

Electrophysiology

Hippocampal slices were prepared as described previously (*30*). Briefly, brains were quickly removed from ether-anesthetized mice and chilled in ice-cold oxygenated artificial cerebrospinal fluid (126 mM NaCl, 5 mM KCl, 26 mM $NaHCO_3$, 2.4 mM $CaCl_2$, 1.3 mM $MgSO_4$, 1.26 mM KH_2PO_4, and 10 mM D-glucose). Transverse hippocampal slices (400 μm thickness) were cut using a vibratome (Microslicer DTK-1000, Dosaka EM) and transferred to a recording chamber, where they were allowed to recover for at least 1 hour at 34°C before recording. Artificial cerebrospinal fluid maintained at 34°C was used during the experiment. A concentric bipolar stimulating electrode was placed in the stratum radiatum of CA1 to stimulate the Schaffer collateral pathway. An HFS of 100 Hz with a 1-s duration was applied twice with a 20-s interval. Traces were digitized with an A/D converter (PowerLab 200, AD Instruments) and computer (Windows, Measurement and Analysis System for LTP: FAL-3000). For whole-cell patch clamp recording, sEPSCs were recorded at room temperature (22° to 25°C) for cultured neurons on DIV21 using an EPC10 amplifier (HEKA, Lambrecht/Pfalz, Germany). The following buffers were used: extracellular buffer (143 mM NaCl, 5 mM KCl, 2 mM $CaCl_2$, 1 mM $MgCl_2$, 10 mM glucose, and 10 mM Hepes at pH 7.4 adjusted with NaOH) and intracellular buffer (135 mM CsMeS, 5 mM CsCl, 10 mM Hepes, 0.5 mM EGTA, 1 mM $MgCl_2$, 4 mM Mg_2ATP, and 0.4 mM NaGTP at pH 7.4 adjusted with CsOH). Recording pipettes were made of borosilicate glass (B150-86-10, Sutter Instruments) and had a resistance of 3.5 to 4.5 megaohm when filled with intracellular buffer. The sEPSCs were recorded for 2 min at a holding potential of −70 mV in the presence of 20 μM bicuculline in the extracellular buffer to block γ-aminobutyric acid type A receptors. Recordings were filtered at 2 kHz and digitized at 10 kHz. Access resistances were monitored throughout the experiment (<15 megohm) but not compensated. Data were collected and initially analyzed using Patchmaster software (HEKA). Further analysis was performed using IgorPRO version 6.3 (Wavemetrics, Portland, OR, USA), Excel (Microsoft), and MiniAnalysis programs version 6.0.7.

Drugs

5-ALA (Cosmo Bio) and sodium ferrous citrate were provided by SBI Pharmaceuticals. PpIX was purchased from Sigma-Aldrich. CGG-KI mice were randomized into three groups for drug administration. For the 5-ALA treatment, 5-ALA [1 and 3 mg/kg, p.o. with sodium ferrous citrate (20:1 molar ratio) dissolved in distilled water] or vehicle (sodium ferrous citrate dissolved in distilled water) was administered daily when mice were 50 to 54 weeks old.

Behavioral analysis

Mice were subjected to behavioral tests, including the Y-maze, Barnes-maze, and beam-walking tasks. All behavioral experiments were conducted with the experimenter blinded to mouse genotype and treatment. Behavioral tests were conducted in an isolated room under dim light between 8:30 a.m. and 8:30 p.m. To measure locomotor activity during a 24-hour period, mice were individually housed in standard plastic cages positioned in an automated open-field activity monitor using digital counters with an infrared sensor (DAS system, Neuroscience). In the Y-maze, spontaneous alternation behavior was assessed as a task for spatial reference memory. The apparatus consisted of three identical arms (50 cm by 16 cm by 32 cm) of black plexiglass. Mice were placed at the end of one arm and allowed to move freely through the maze for an 8-min session. The sequence of arm entries was manually recorded. An alternation was defined as entries into all three arms on consecutive choices. The maximum number of alternations was defined as the total number of arms entered minus two, and the percentage of alternations was calculated as actual alternations/maximum alternations × 100. The total number of arms entered during the session was also determined. The Barnes-maze task was designed to test spatial learning and memory in rodents. It consists of a circular platform 92 cm in diameter with 20 5-cm holes along the perimeter. At the beginning of each trial, the mouse is placed in the middle of the maze in a cylindrical 7.5-cm start chamber. After 10 s, the chamber is lifted, and the mouse is free to explore the maze. The test ends when the mouse enters the goal

tunnel or after 3 min have elapsed. Immediately after the mouse enters the tunnel, the mouse is allowed to stay in the tunnel for 1 min. Mice were trained for two trials per day for 4 days. The search time required to escape into the tunnel was recorded. In the beam-walking task, the apparatus consisted of a rectangular beam (870 mm by 5 mm) and goal box (155 mm by 160 mm by 5 mm). Both ends of the beam were fixed at 500 and 315 mm from the floor, and the goal box was placed on the higher end of the beam. The number of foot slips (i.e., missteps) from the end of the beam to the goal box was recorded.

Statistical analysis

We followed the standard sample sizes used in similar experiments in each of the relevant fields reported in the literature. All values are expressed as means ± SEM. Statistical significance for differences among groups was tested by one-way or two-way analysis of variance (ANOVA) with post hoc Bonferroni's multiple comparison test. Comparisons between two experimental groups were made using the two-sided, unpaired Student's *t* test. Comparisons between two groups in distributions of sEPSCs amplitudes were made using the Kolmogorov-Smirnov test. $P < 0.05$ was considered significant. All the statistical analyses were performed using GraphPad Prism 7 (GraphPad Software). Source data are provided in table S3. Full-size scans of Western blots are shown in fig. S6.

SUPPLEMENTARY MATERIALS

Supplementary material for this article is available at http://advances.sciencemag.org/cgi/content/full/7/3/eabd9440/DC1

View/request a protocol for this paper from *Bio-protocol*.

REFERENCES AND NOTES

1. R. J. Hagerman, M. Leehey, W. Heinrichs, F. Tassone, R. Wilson, J. Hills, J. Grigsby, B. Gage, P. J. Hagerman, Intention tremor, parkinsonism, and generalized brain atrophy in male carriers of fragile X. *Neurology* **57**, 127–130 (2001).
2. R. J. Hagerman, P. Hagerman, Fragile X-associated tremor/ataxia syndrome - features, mechanisms and management. *Nat. Rev. Neurol.* **12**, 403–412 (2016).
3. S. Jacquemont, R. J. Hagerman, M. A. Leehey, D. A. Hall, R. A. Levine, J. A. Brunberg, L. Zhang, T. Jardini, L. W. Gane, S. W. Harris, K. Herman, J. Grigsby, C. M. Greco, E. Berry-Kravis, F. Tassone, P. J. Hagerman, Penetrance of the fragile X-associated tremor/ataxia syndrome in a premutation carrier population. *JAMA* **91**, 460–469 (2004).
4. O. A. Sofola, P. Jin, Y. Qin, R. Duan, H. Liu, M. de Haro, D. L. Nelson, J. Botas, RNA-binding proteins hnRNP A2/B1 and CUGBP1 suppress fragile X CGG premutation repeat-induced neurodegeneration in a Drosophila model of FXTAS. *Neuron* **55**, 565–571 (2007).
5. C. Sellier, F. Rau, Y. Liu, F. Tassone, R. K. Hukema, R. Gattoni, A. Schneider, S. Richard, R. Willemsen, D. J. Elliott, P. J. Hagerman, N. Charlet-Berguerand, Sam68 sequestration and partial loss of function are associated with splicing alterations in FXTAS patients. *EMBO J.* **29**, 1248–1261 (2010).
6. C. Sellier, F. Freyermuth, R. Tabet, T. Tran, F. He, F. Ruffenach, V. Alunni, H. Moine, C. Thibault, A. Page, F. Tassone, R. Willemsen, M. D. Disney, P. J. Hagerman, P. K. Todd, N. Charlet-Berguerand, Sequestration of DROSHA and DGCR8 by expanded CGG RNA repeats alters microRNA processing in fragile X-associated tremor/ataxia syndrome. *Cell Rep.* **3**, 869–880 (2013).
7. F. He, A. Krans, B. D. Freibaum, J. P. Taylor, P. K. Todd, TDP-43 suppresses CGG repeat-induced neurotoxicity through interactions with HnRNP A2/B1. *Hum. Mol. Genet.* **23**, 5036–5051 (2014).
8. C. M. Greco, R. J. Hagerman, F. Tassone, A. E. Chudley, M. R. Del Bigio, S. Jacquemont, M. Leehey, P. J. Hagerman, Neuronal intranuclear inclusions in a new cerebellar tremor/ataxia syndrome among fragile X carriers. *Brain* **125**, 1760–1771 (2002).
9. C. M. Greco, R. F. Berman, R. M. Martin, F. Tassone, P. H. Schwartz, A. Chang, B. D. Trapp, C. Iwahashi, J. Brunberg, J. Grigsby, D. Hessl, E. J. Becker, J. Papazian, M. A. Leehey, R. J. Hagerman, P. J. Hagerman, Neuropathology of fragile X-associated tremor/ataxia syndrome (FXTAS). *Brain* **129**, 243–255 (2006).
10. C. K. Iwahashi, D. H. Yasui, H.-J. An, C. M. Greco, F. Tassone, K. Nannen, B. Babineau, C. B. Lebrilla, R. J. Hagerman, P. J. Hagerman, Protein composition of the intranuclear inclusions of FXTAS. *Brain* **129**, 256–271 (2006).
11. P. K. Todd, S. Y. Oh, A. Krans, F. He, C. Sellier, M. Frazer, A. J. Renoux, K. Chen, K. M. Scaglione, V. Basrur, K. Elenitoba-Johnson, J. P. Vonsattel, E. D. Louis, M. A. Sutton, J. P. Taylor, R. E. Mills, N. Charlet-Berguerand, H. L. Paulson, CGG repeat-associated translation mediates neurodegeneration in fragile X tremor ataxia syndrome. *Neuron* **78**, 440–455 (2013).
12. M. G. Kearse, K. M. Green, A. Krans, C. M. Rodriguez, A. E. Linsalata, A. C. Goldstrohm, P. K. Todd, CGG repeat-associated non-AUG translation utilizes a Cap-dependent scanning mechanism of initiation to produce toxic proteins. *Mol. Cell* **62**, 314–322 (2016).
13. A. Krans, M. G. Kearse, P. K. Todd, Repeat-associated non-AUG translation from antisense CCG repeats in fragile X tremor/ataxia syndrome. *Ann. Neurol.* **80**, 871–881 (2016).
14. A. Krans, G. Skariah, Y. Zhang, B. Bayly, P. K. Todd, Neuropathology of RAN translation proteins in fragile X-associated tremor/ataxia syndrome. *Acta Neuropathol. Commun.* **7**, 152 (2019).
15. C. Sellier, R. A. M. Buijsen, F. He, S. Natla, L. Jung, P. Tropel, A. Gaucherot, H. Jacobs, H. Meziane, A. Vincent, M. Champy, T. Sorg, G. Pavlovic, M. Wattenhofer-Donze, M. Birling, M. Oulad-Abdelghani, P. Eberling, F. Ruffenach, M. Joint, M. Anheim, V. Martinez-Cerdeno, F. Tassone, R. Willemsen, R. K. Hukema, S. Viville, C. Martinat, P. K. Todd, N. Charlet-Berguerand, Translation of expanded CGG repeats into FMRpolyG is pathogenic and may contribute to fragile X tremor ataxia syndrome. *Neuron* **93**, 331–347 (2017).
16. R. A. M. Buijsen, C. Sellier, L. W. F. M. Severijnen, M. Oulad-Abdelghani, R. F. M. Verhagen, R. F. Berman, N. Charlet-Berguerand, R. Willemsen, R. K. Hukema, FMRpolyG-positive inclusions in CNS and non-CNS organs of a fragile X premutation carrier with fragile X-associated tremor/ataxia syndrome. *Acta Neuropathol. Commun.* **2**, 162 (2014).
17. R. A. M. Buijsen, J. A. Visser, P. Kramer, L. A. W. F. M. Severijnen, M. Gearing, N. Charlet-Berguerand, S. L. Sherman, R. F. Berman, R. Willemsen, R. K. Hukema, Presence of inclusions positive for polyglycine containing protein, FMRpolyG, indicates that repeat-associated non-AUG translation plays a role in fragile X-associated primary ovarian insufficiency. *Hum. Reprod.* **31**, 158–168 (2015).
18. P. Romero, Z. Obradovic, X. Li, E. C. Garner, C. J. Brown, A. K. Dunker, Sequence complexity of disordered protein. *Proteins* **42**, 38–48 (2001).
19. A. K. Lancaster, A. Nutter-Upham, S. Lindquist, O. D. King, PLAAC: a web and command-line application to identify proteins with prion-like amino acid composition. *Bioinformatics* **30**, 2501–2502 (2014).
20. D. J. Abraham, A. J. Leo, Extension of the fragment method to calculate amino acid zwitterion and side chain partition coefficients. *Proteins* **2**, 130–152 (1987).
21. A. Ciesiolka, M. Jazurek, K. Drazkowska, W. J. Krzyzosiak, Structural characteristics of simple RNA repeats associated with disease and their deleterious protein interactions. *Front. Cell. Neurosci.* **11**, 97 (2017).
22. X. Wang, K. J. Goodrich, E. G. Conlon, J. Gao, A. H. Erbse, J. L. Manley, T. R. Cech, C9orf72 and triplet repeat disorder RNAs: G-quadruplex formation, binding to PRC2 and implications for disease mechanisms. *RNA* **25**, 935–947 (2019).
23. A. A. Hyman, C. A. Weber, F. Jülicher, Liquid-liquid phase separation in biology. *Annu. Rev. Cell Dev. Biol.* **30**, 39–58 (2014).
24. S. Boeynaems, S. Alberti, N. L. Fawzi, T. Mittag, M. Polymenidou, F. Rousseau, J. Schymkowitz, J. Shorter, B. Wolozin, L. Van Den Bosch, P. Tompa, M. Fuxreiter, Protein phase separation: A new phase in cell biology. *Trends Cell Biol.* **28**, 420–435 (2018).
25. Y. Lin, E. Mori, M. Kato, S. Xiang, L. Wu, I. Kwon, S. L. McKnight, Toxic PR poly-dipeptides encoded by the C9orf72 repeat expansion target LC domain polymers. *Cell* **167**, 789–802. e12 (2016).
26. S. Keerthikumar, D. Chisanga, D. Ariyaratne, H. A. Saffar, S. Anand, K. Zhao, M. Samuel, M. Pathan, M. Jois, N. Chilamkurti, L. Gangoda, S. Mathivanan, ExoCarta: A Web-based compendium of exosomal cargo. *J. Mol. Biol.* **428**, 688–692 (2016).
27. C. Peng, J. Q. Trojanowski, V. M.-Y. Lee, Protein transmission in neurodegenerative disease. *Nat. Rev. Neurol.* **16**, 199–212 (2020).
28. Z. Cao, S. Hulsizer, F. Tassone, H. Tang, R. J. Hagerman, M. A. Rogawski, P. J. Hagerman, I. N. Pessah, Clustered burst firing in FMR1 premutation hippocampal neurons: amelioration with allopregnanolone. *Hum. Mol. Genet.* **21**, 2923–2935 (2012).
29. G. Robin, J. R. López, G. M. Espinal, S. Hulsizer, P. J. Hagerman, I. N. Pessah, Calcium dysregulation and Cdk5-ATM pathway involved in a mouse model of fragile X-associated tremor/ataxia syndrome. *Hum. Mol. Genet.* **26**, 2649–2666 (2017).
30. N. Shioda, Y. Yabuki, K. Yamaguchi, M. Onozato, Y. Li, K. Kurosawa, H. Tanabe, N. Okamoto, T. Era, H. Sugiyama, T. Wada, K. Fukunaga, Targeting G-quadruplex DNA as cognitive function therapy for ATR-X syndrome. *Nat. Med.* **24**, 802–813 (2018).
31. T. Wada, S. Suzuki, N. Shioda, 5-Aminolevulinic acid can ameliorate language dysfunction of patients with ATR-X syndrome. *Congenit. Anom. (Kyoto)* **60**, 147–148 (2020).
32. M. G. Nasab, L. Hassani, S. M. Nejad, D. Norouzi, Interaction of hemin with quadruplex DNA. *J. Biol. Physiol.* **43**, 5–14 (2017).
33. K. M. Green, U. J. Sheth, B. N. Flores, S. E. Wright, A. B. Sutter, M. G. Kearse, S. J. Barmada, M. I. Ivanova, P. K. Todd, High-throughput screening yields several small-molecule inhibitors of repeat-associated non-AUG translation. *J. Biol. Chem.* **294**, 18624–18638 (2019).

34. M. R. Hunsaker, K. Kim, R. Willemsen, R. F. Berman, CGG trinucleotide repeat length modulates neural plasticity and spatiotemporal processing in a mouse model of the fragile X premutation. *Hippocampus* **22**, 2260–2275 (2012).
35. D. Kumari, M. Swaroop, N. Southall, W. Huang, W. Zheng, K. Usdin, High-throughput screening to identify compounds that increase fragile X mental retardation protein expression in neural stem cells differentiated from fragile X syndrome patient-derived induced pluripotent stem cells. *Stem Cells Transl. Med.* **4**, 800–808 (2015).
36. C. M. Rodriguez, S. E. Wright, M. G. Kearse, J. M. Haenfler, B. N. Flores, Y. Liu, M. F. Ifrim, M. R. Glineburg, A. Krans, P. Jafar-Nejad, M. A. Sutton, G. J. Bassell, J. M. Parent, F. Rigo, S. J. Barmada, P. K. Todd, A native function for RAN translation and CGG repeats in regulating fragile X protein synthesis. *Nat. Neurosci.* **23**, 386–397 (2020).
37. M. Kato, T. W. Han, S. Xie, K. Shi, X. Du, L. C. Wu, H. Mirzaei, E. J. Goldsmith, J. Longgood, J. Pei, N. V. Grishin, D. E. Frantz, J. W. Schneider, S. Chen, L. Li, M. R. Sawaya, D. Eisenberg, R. Tycko, S. L. McKnight, Cell-free formation of RNA granules: low complexity sequence domains form dynamic fibers within hydrogels. *Cell* **149**, 753–767 (2012).
38. Y. Lin, D. S. Protter, M. K. Rosen, R. Parker, Formation and maturation of phase-separated liquid droplets by RNA-binding proteins. *Mol. Cell* **60**, 208–219 (2015).
39. A. Jain, R. D. Vale, RNA phase transitions in repeat expansion disorders. *Nature* **546**, 243–247 (2017).
40. B. Van Treeck, D. S. W. Protter, T. Matheny, A. Khong, C. D. Link, R. Parker, RNA self-assembly contributes to stress granule formation and defining the stress granule transcriptome. *Proc. Natl. Acad. Sci. U.S.A.* **115**, 2734–2739 (2018).
41. S. Xiang, M. Kato, L. C. Wu, Y. Lin, M. Ding, Y. Zhang, Y. Yu, S. L. McKnight, The LC domain of hnRNPA2 adopts similar conformations in hydrogel polymers, liquid-like droplets, and nuclei. *Cell* **163**, 829–839 (2015).
42. A. Patel, H. O. Lee, L. Jawerth, S. Maharana, M. Jahnel, M. Y. Hein, S. Stoynov, J. Mahamid, S. Saha, T. M. Franzmann, A. Pozniakovski, I. Poser, N. Maghelli, L. A. Royer, M. Weigert, E. W. Myers, S. Grill, D. Drechsel, A. A. Hyman, S. Alberti, A liquid-to-solid phase transition of the ALS protein FUS accelerated by disease mutation. *Cell* **162**, 1066–1077 (2015).
43. A. Molliex, J. Temirov, J. Lee, M. Coughlin, A. P. Kanagaraj, H. J. Kim, T. Mittag, J. P. Taylor, Phase separation by low complexity domains promotes stress granule assembly and drives pathological fibrillization. *Cell* **163**, 123–133 (2015).
44. S. Ambadipudi, J. Biernat, D. Riedel, E. Mandelkow, M. Zweckstetter, Liquid-liquid phase separation of the microtubule-binding repeats of the Alzheimer-related protein Tau. *Nat. Commun.* **8**, 275 (2017).
45. O. D. King, A. D. Gitler, J. Shorter, The tip of the iceberg: RNA-binding proteins with prion-like domains in neurodegenerative disease. *Brain Res.* **1462**, 61–80 (2012).
46. H. Ishiura, S. Shibata, J. Yoshimura, Y. Suzuki, W. Qu, K. Doi, M. A. Almansour, J. K. Kikuchi, M. Taira, J. Mitsui, Y. Takahashi, Y. Ichikawa, T. Mano, A. Iwata, Y. Harigaya, M. K. Matsukawa, T. Matsukawa, M. Tanaka, Y. Shirota, R. Ohtomo, H. Kowa, H. Date, A. Mitsue, H. Hatsuta, S. Morimoto, S. Murayama, Y. Shiio, Y. Saito, A. Mitsutake, M. Kawai, T. Sasaki, Y. Sugiyama, M. Hamada, G. Ohtomo, Y. Terao, Y. Nakazato, A. Takeda, Y. Sakiyama, Y. Umeda-Kameyama, J. Shinmi, K. Ogata, Y. Kohno, S. Lim, A. H. Tan, J. Shimizu, J. Goto, I. Nishino, T. Toda, S. Morishita, S. Tsuji, Noncoding CGG repeat expansions in neuronal intranuclear inclusion disease, oculopharyngodistal myopathy and an overlapping disease. *Nat. Genet.* **51**, 1222–1232 (2019).
47. J. Sone, S. Mitsuhashi, A. Fujita, T. Mizuguchi, K. Hamanaka, K. Mori, H. Koike, A. Hashiguchi, H. Takashima, H. Sugiyama, Y. Kohno, Y. Takiyama, K. Maeda, H. Doi, S. Koyano, H. Takeuchi, M. Kawamoto, N. Kohara, T. Ando, T. Ieda, Y. Kita, N. Kokubun, Y. Tsuboi, K. Katoh, Y. Kino, M. Katsuno, Y. Iwasaki, M. Yoshida, F. Tanaka, I. K. Suzuki, M. C. Frith, N. Matsumoto, G. Sobue, Long-read sequencing identifies GGC repeat expansions in NOTCH2NLC associated with neuronal intranuclear inclusion disease. *Nat. Genet.* **51**, 1215–1221 (2019).
48. F. Clavaguera, J. Hench, I. Lavenir, G. Schweighauser, S. Frank, M. Goedert, M. Tolnay, Peripheral administration of tau aggregates triggers intracerebral tauopathy in transgenic mice. *Acta Neuropathol.* **127**, 299–301 (2014).
49. E. Luna, S. C. Decker, D. M. Riddle, A. Caputo, B. Zhang, T. Cole, C. Caswell, S. X. Xie, V. M. Y. Lee, K. C. Luk, Differential α-synuclein expression contributes to selective vulnerability of hippocampal neuron subpopulations to fibril- induced toxicity. *Acta Neuropathol.* **135**, 855–875 (2018).
50. S. Alberti, R. Halfmann, O. King, A. Kapila, S. A. Lindquist, A systematic survey identifies prions and illuminates sequence features of prionogenic proteins. *Cell* **137**, 146–158 (2009).
51. S. Liu, A. Hossinger, S. Göbbels, I. M. Vorberg, Prions on the run: How extracellular vesicles serve as delivery vehicles for self-templating protein aggregates. *Prion* **11**, 98–112 (2017).
52. C. Villarroya-Beltri, C. Vazquez-Salinas, F. Madrid, D. Hernandez, J. Vázquez, N. Martin, D. J. Herrera, A. Pascual-Montano, M. Mittelbrunn, F. Sánchez-Madrid, Sumoylated hnRNPA2B1 controls the sorting of miRNAs into exosomes through binding to specific motifs. *Nat. Commun.* **4**, 2980 (2013).
53. H. Jürgen Wenzel, K. D. Murray, S. N. Haify, M. R. Hunsaker, J. J. Schwartzer, K. Kim, A. R. La Spada, B. L. Sopher, P. J. Hagerman, C. Raske, L. W. F. M. Severijnen, R. Willemsen, R. K. Hukema, R. F. Berman, Astroglial-targeted expression of the fragile X CGG repeat premutation in mice yields RAN translation, motor deficits and possible evidence for cell-to-cell propagation of FXTAS pathology. *Acta Neuropathol. Commun.* **7**, 27 (2019).
54. P. Murat, G. Marsico, B. Herdy, A. T. Ghanbarian, G. Portella, S. Balasubramanian, RNA G-quadruplexes at upstream open reading frames cause DHX36- and DHX9-dependent translation of human mRNAs. *Genome Biol.* **19**, 229 (2018).
55. S. Asamitsu, S. Obata, Z. Yu, T. Bando, H. Sugiyama, Recent progress of targeted G-quadruplex-preferred ligands toward cancer therapy. *Molecules* **24**, 429 (2019).
56. M. DeJesus-Hernandez, I. R. Mackenzie, B. F. Boeve, A. L. Boxer, M. Baker, N. J. Rutherford, A. M. Nicholson, N. A. Finch, H. Flynn, J. Adamson, N. Kouri, A. Wojtas, P. Sengdy, G. R. Hsiung, A. Karydas, W. W. Seeley, K. A. Josephs, G. Coppola, D. H. Geschwind, Z. K. Wszolek, H. Feldman, D. S. Knopman, R. C. Petersen, B. L. Miller, D. W. Dickson, K. B. Boylan, N. R. Graff-Radford, R. Rademakers, Expanded GGGGCC hexanucleotide repeat in noncoding region of C9ORF72 causes chromosome 9p-linked FTD and ALS. *Neuron* **72**, 245–256 (2011).
57. A. E. Renton, E. Majounie, A. Waite, J. Simón-Sánchez, S. Rollinson, J. R. Gibbs, J. C. Schymick, H. Laaksovirta, J. C. van Swieten, L. Myllykangas, H. Kalimo, A. Paetau, Y. Abramzon, A. M. Remes, A. Kaganovich, S. W. Scholz, J. Duckworth, J. Ding, D. W. Harmer, D. G. Hernandez, J. O. Johnson, K. Mok, M. Ryten, D. Trabzuni, R. J. Guerreiro, R. W. Orrell, J. Neal, A. Murray, J. Pearson, I. E. Jansen, D. Sondervan, H. Seelaar, D. Blake, K. Young, N. Halliwell, J. B. Callister, G. Toulson, A. Richardson, A. Gerhard, J. Snowden, D. Mann, D. Neary, M. A. Nalls, T. Peuralinna, L. Jansson, V. Isoviita, A. Kaivorinne, M. Hölttä-Vuori, E. Ikonen, R. Sulkava, M. Benatar, J. Wuu, A. Chiò, G. Restagno, G. Borghero, M. Sabatelli; ITALSGEN Consortium, D. Heckerman, E. Rogaeva, L. Zinman, J. D. Rothstein, M. Sendtner, C. Drepper, E. E. Eichler, C. Alkan, Z. Abdullaev, S. D. Pack, A. Dutra, E. Pak, J. Hardy, A. Singleton, N. M. Williams, P. Heutink, S. Pickering-Brown, H. R. Morris, P. J. Tienari, B. J. Traynor, A hexanucleotide repeat expansion in C9ORF72 is the cause of chromosome 9p21-linked ALS-FTD. *Neuron* **72**, 257–268 (2011).
58. C. J. M. Bontekoe, C. E. Bakker, I. M. Nieuwenhuizen, H. van der Linde, H. Lans, D. de Lange, M. C. Hirst, B. A. Oostra, Instability of a $(CGG)_{98}$ repeat in the Fmr1 promoter. *Hum. Mol. Genet.* **10**, 1693–1699 (2001).
59. R. K. Hukema, B. A. Oostra, The CGG repeat and the FMR1 gene. *Methods Mol. Biol.* **1010**, 155–176 (2013).
60. S. Asamitsu, Y. Imai, Y. Yabuki, S. Ikenoshita, M. Takeuchi, H. Kashiwagi, Y. Tanoue, T. Fukuda, N. Shioda, Identification and immunohistochemical characterization of G-quadruplexes in mouse brain. *Biochem. Biophys. Res. Commun.* **531**, 67–74 (2020).
61. M. Grey, C. J. Dunning, R. Gaspar, C. Grey, P. Brundin, E. Sparr, S. Linse, Acceleration of α-synuclein aggregation by exosomes. *J. Biol. Chem.* **290**, 2969–2982 (2015).

Acknowledgments: We thank R. Willemsen (Erasmus MC Rotterdam, The Netherlands) for providing the CGG-KI mouse line and P. K. Todd (University of Michigan Medical School, USA) for providing the FMRpolyG-NL and ATG-NL plasmids. **Funding:** This research was supported by AMED (grant numbers JP19ek0109235 and JP20ek0109425 to N.S.), JSPS KAKENHI (grant numbers JP20K15417 and JP20J00520 to S.A.; JP19K16369 to Y.Y.; and JP16K08265, JP19H05221, and JP20H03393 to N.S.), the Astellas Foundation for Research on Metabolic Disorders (to N.S.), the Daiichi-Sankyo Foundation of Life Science (to N.S.), the Kanae Foundation for the Promotion of Medical Science (to N.S.); the Mitsubishi Foundation (to N.S.), and the program of the Joint Usage/Research Center for Developmental Medicine, Institute of Molecular Embryology and Genetics, Kumamoto University. **Author contributions:** S.A., Y.Y., S.I., K.K., M.K., S.U., and N.S. performed the experiments. Y.N., K.A., H.K., K.I., T.M., H.S., K.F., and E.N. provided critical advice. S.A., Y.Y., and N.S. wrote the manuscript and designed the study. **Competing interests:** The authors declare that they have no competing interests. **Data and materials availability:** A summary of all statistical data are shown in table S3. The raw RNA sequencing data are available at DRA010402. Additional data related to this paper may be requested from the corresponding author upon reasonable request. The 5′-UTR-CGG×99-FMR1-EGFP plasmid can be provided by Addgene pending scientific review and a completed material transfer agreement. Requests for the 5′-UTR–CGG×99-FMR1-EGFP plasmid should be submitted to Addgene.

Submitted 21 July 2020
Accepted 18 November 2020
Published 13 January 2021
10.1126/sciadv.abd9440

Citation: S. Asamitsu, Y. Yabuki, S. Ikenoshita, K. Kawakubo, M. Kawasaki, S. Usuki, Y. Nakayama, K. Adachi, H. Kugoh, K. Ishii, T. Matsuura, E. Nanba, H. Sugiyama, K. Fukunaga, N. Shioda, CGG repeat RNA G-quadruplexes interact with FMRpolyG to cause neuronal dysfunction in fragile X-related tremor/ataxia syndrome. *Sci. Adv.* **7**, eabd9440 (2021).